Micron 158 (2022) 103292

Contents lists available at ScienceDirect

Micron

journal homepage: www.elsevier.com/locate/micron

Effectiveness of X-ray micro-CT applications upon mafic and ultramafic ophiolitic rocks

Vasileios Giamas [a,b], Petros Koutsovitis [a,*], Alkiviadis Sideridis [a], Pascal Turberg [c], Tassos A. Grammatikopoulos [d], Petros Petrounias [a], Panagiota P. Giannakopoulou [a], Nikolaos Koukouzas [b], Konstantin Hatzipanagiotou [a]

[a] University of Patras (UoP), Department of Geology, Section of Earth Materials, 26504 Rio, Greece
[b] Centre for Research and Technology, Hellas (CERTH), 15125 Marousi, Greece
[c] École Polytechnique Fédérale de Lausanne EPFL, School of Architecture, Civil and Environmental Engineering ENAC, Civil Engineering Institute IIC, Lausanne, Switzerland
[d] SGS Canada Inc, 185 Concession St., Lakefield, ON K0L 2H0, Canada

ARTICLE INFO

Keywords:
Ophiolites
Applied petrography
Micro-computed tomography (μCT)
Modal composition
3D rock fabric

ABSTRACT

X-ray micro-computed tomography (μCT) was applied upon selected ophiolitic rock samples from various localities of the Vardar ophiolite outcrops in North Greece. Effectiveness of the μCT application was evaluated through this case study by comparing results with other state-of-the-art techniques (e.g., optical microscopy, mineral chemistry microanalyses, XRD and QEMSCAN) to provide suggestive methodologies for optimum characterization, geological modeling, and visualization of ophiolitic rocks. The research outcomes provide an innovative approach for accurate modal composition calculations, crystal structure and mineral distribution in a 3D perspective, by combining μCT results with mineral chemical analyses. The information obtained is critical for investigating ophiolitic rocks to resolve complex petrogenetic and post-magmatic phenomena, to identify fabrics related to deformation, and furthermore results can also be used for applied research purposes. The obtained μCT results suggest that distributions of mineral's grayscale values strongly rely on three key factors: (i) participation of mineral phases with distinct attenuation coefficient and/or density properties, (ii) coexistence of different mafic minerals or mafic with non-mafic phases, (iii) variability in their mineral chemistry. The ability to analyze and visualize the internal mineral constituents of ophiolitic rocks samples, through the combination of μCT and Energy-Dispersive X-ray spectroscopy (EDS), can lead to advanced 3D stereological rock fabric analyses, which is advantageous compared to 2D methodologies. The μCT allowed to perform rock fabric calculations (best-fit ellipsoids and with volume) upon specified grain size distributions to identify and characterize the 3D morphological properties of the participating crystals and their preferable orientation.

1. Introduction

Ophiolites represent fragments of oceanic crust and lithospheric mantle that have been over-thrusted above continental crustal rocks and terrains (Dilek and Furnes, 2011; Rassios et al., 2020; Whattam and Stern, 2011). A typical ophiolitic sequence comprises successive lithostratigraphic sections of ultramafics, gabbros, sheeted dikes, pillow lavas and layered deep-sea sediments from bottom to top. Ophiolites participate in orogenetic cycles and are overthrusted during the closure of oceanic basins. Even though members of an ideal ophiolitic sequence are well defined, they often crop out as dismembered ophiolitic units, varying significantly in terms of petrographic features, mineralogical properties, and geochemical patterns (Dilek et al., 2008; Koutsovitis, 2012; Rassios et al., 2020). These differences are mostly due to factors that include the geotectonic environment of formation; whether they represent for-arc or back-arc ophiolites, and petrogenetic conditions that occurred deep within the mantle and in the magma chamber during differentiation, assimilation, and crystallization (Bortolotti et al., 2013; Magganas and Koutsovitis, 2015).

To assess the petrogenetic processes that led to the formation of ophiolitic complexes and to identify secondary metasomatic processes, research efforts were focused on determining the modal composition

* Corresponding author.
E-mail address: pkoutsovitis@upatras.gr (P. Koutsovitis).

https://doi.org/10.1016/j.micron.2022.103292
Received 22 December 2021; Received in revised form 7 April 2022; Accepted 23 April 2022
Available online 30 April 2022

and textural features ophiolitic rocks by applying state-of-the-art techniques including optical microscopy, mineral chemistry microanalyses, X-ray diffraction analyses (XRD) and QEMSCAN (Al-Khirbash, 2020; Grammatikopoulos et al., 2011; Ishimaru et al., 2017; Magganas and Koutsovitis, 2015; Mayhew et al., 2018; Miller et al., 2017; Šegvić et al., 2016; Tilhac et al., 2016; Zoheir et al., 2022). Despite the advantages of the aforementioned techniques, the main drawback is that results are based upon "two dimensional" data (thin section slices) hindering the ability to precisely determine modal composition and grain size of the mineral phases, as well as textural and crystal structure information from a three-dimensional perspective. To overcome this barrier, computational techniques such as MINSQ (Herrmann and Berry, 2002) that combine geochemical results with mineral chemistry analyses, have been proven to provide fairly accurate modal composition calculations. However, accuracy of these techniques strongly depends on the number of mineral phases; small number of mineral phases leads to more precise results.

X-ray micro–Computed Tomography (μCT) is a technique that has been introduced in medical sciences (Langheinrich et al., 2004; Sarno et al., 2016), archeology (Huisman et al., 2014; Ngan-Tillard et al., 2018; Tuniz and Zanini, 2018), material sciences (Mehdikhani et al., 2019; Schladitz, 2011), engineering (Fang et al., 2019; Yang and Elhajjar, 2014) and geosciences (Carlson et al., 2003; Cnudde and Boone, 2013; Hanna and Ketcham, 2017; Ketcham and Carlson, 2001). Application of μCT enables the non-destructive, 3D visualization of internal phases hosted within a rock sample. Geological samples have been studied using this technique, including igneous rocks (Baker et al., 2012; Boone et al., 2011; Callow et al., 2018; Cid et al., 2017; Jardine et al., 2018), sedimentary rocks/sediment cores (Christe et al., 2011; De Boever et al., 2015; Emmanouilidis et al., 2020; Lai et al., 2017; Munawar et al., 2018; Zhang et al., 2019), peat and soils (Le Bayon et al., 2021; Liernur et al., 2017; Turberg et al., 2014), metamorphic rocks (Aerden and Ruiz-Fuentes, 2020; Corti et al., 2019; Sayab et al., 2021, 2017; Zucali et al., 2014), ore/drill cores (Godel, 2013; Kyle and Ketcham, 2015; Reyes et al., 2017; Sahiström et al., 2019; Warlo et al., 2021) and meteorites (Friedrich et al., 2008; Porfido et al., 2020; Tsuchiyama et al., 2002; Uesugi et al., 2010). To our knowledge ophiolitic rocks have not been extensively examined using μCT applications, although there are a few cases reported concerning ophiolitic chromitites (Prichard et al., 2017, 2018, 2015), as well as serpentinized and carbonatized ultramafic rocks (Beinlich et al., 2020; Noël et al., 2018). Two pyroxene-bearing gabbro samples, one from Chile (Gomila et al., 2019) and another (likely ophiolitic) from the Southern Alps (Petri et al., 2020) were also examined using μCT whereas from mantle-related rocks, only mantle xenoliths have been considered (Bhanot et al., 2017; Horton et al., 2019; Howarth et al., 2015; Kuper et al., 2007; Patkó et al., 2020). Although μCT has been applied to different rock types, discrimination amongst the participating silicate minerals is vague compared to other state-of-the-art techniques.

Aim of this study is to evaluate the applicability of μCT upon relatively unaltered ophiolitic rocks and to provide suggestive methodologies that can be implemented for optimum characterization, geological modeling, and visualization of ophiolitic rocks to assist in resolving specific geological or geoengineering queries where ophiolites are involved. The results and methodologies presented provide an innovative approach to distinguish amongst principal rock forming minerals, precisely quantify mineral modal abundances, and identify textural features such as those related to deformation associated with post-magmatic metamorphism in three dimensions.

2. Geological setting and sample localities

Ophiolites in Greece crop out throughout its mainland mostly as dispersed ophiolitic thrust sheets. The most important ophiolitic bodies are exposed along with pelagic and abyssal related sedimentary formations in the form of two subparallel zones trending with a NW-SE direction. The ophiolites were emplaced during the closure of the Pindos and Vardar Neotethyan oceanic basins, during the orogenetic periods that include the Upper Jurassic – Lower Cretaceous and the post-Paleocene (Beccaluva et al., 2005; Ferrière et al., 2012). These geotectonic processes were responsible for the extensive serpentinization and metasomatism of many ophiolitic formations and therefore only few localities in Greece have retained relatively fresh lithotypes. For this reason, we chose to sample rocks from relatively well-preserved ophiolites and particularly from the Inner Hellenic Ophiolitic Belt that is exposed in Central Macedonia (Greece). This ophiolitic sequence appears to be dismembered, cropping out along the contact between the Vardar zone and the Circum-Rhodope Belt (Fig. 1a). From north to south this sequence includes the following: (i) Gevgelija Complex, which mainly comprise of gabbroic rocks (e.g., hornblende and/or olivine gabbro) along with volcanic sequences of mafic rocks crosscut by diabase dikes that intrude Fanos granite (Danelian et al., 1996; Zachariadis et al., 2006), (ii) Thessaloniki/Oreokastro Units, which typically contains gabbroic and basaltic extrusive rocks that locally lie on top of a mantle harzburgite tectonite (Michard et al., 1998), (iii) West Chalkidiki ophiolites (localities of Triadi, Vasilika, Vavdos, Gerakini – Ormylia and Metamorphosis), which are mostly comprised of a mantle section consisting of harzburgite and dunite bodies that are locally crosscut by gabbroic and pyroxenitic dikes (Christofides et al., 1994; Sideridis et al., 2018, 2021) and (iv) South Chalkidiki ophiolites (i.e., Kassandra and Sithonia outcrops), which consist of extrusive basaltic volcanics and swarm doleritic dikes, accompanied by restricted gabbroic outcrops (Bonev et al., 2015).

Thirty hand-sized samples of mafic and ultramafic composition were collected from the aforementioned outcrops. These include gabbroic rocks from the Guevgueli (Fig. 1b), as well as ultramafic rocks (i.e., peridotites, pyroxenites, chromitites) and gabbroic rocks from West Chalkidiki ophiolites (Fig. 1c,1d respectively). Since the regionally dismembered ophiolitic units were subjected to alteration processes, samples were collected from carefully selected sites that did not experience extensive alteration.

3. Sampling criteria and analytical techniques

3.1. Sample selection, petrological state-of-the-art techniques

The petrographic examination was conducted by optical microscopy upon polished thin sections from all samples to identify the mineral phases and textural features and to evaluate the extent of alteration based on the presence and percentage of secondary minerals (e.g., serpentine, fibrous amphiboles and chlorite). Polished thin sections were prepared at the Research Laboratory of Rocks and Minerals of the University of Patras (UoP). The petrographic examination was performed using a Leitz Ortholux II POL-BK polarized light microscope coupled with a Jenoptik ProgRes® C3 CCD camera. ProgRes® CapturePro software was used to obtain photomicrographs. To determine the most appropriate samples for the purposes of our study, we performed detailed petrographic examination selecting by the following criteria: (i) representative lithotypes, (ii) alteration/metasomatism (minimal and moderate degrees) (iii) restricted number of participating minerals (maximum three major mineral phases), (iv) primary mineral constituents with different densities and attenuation coefficient properties, (v) variability in grain size distribution from a set of samples, (vi) textural homogeneous features within each sample. Following the aforementioned set of criteria, we considered six carefully selected rock samples, which include: two mafic rocks (a gabbronorite and a hornblende microgabbro), three ultramafic rocks (a wehrlite, a hartzburgite, a serpentinized dunite) and a semi-massive chromitite (Cr-ore). Modal composition was initially determined through optical microscopy point-counting technique, based upon ~1000 point counts for each thin section on areas of ~10 cm^2 (see Table 1) using JMicroVision software (Roduit, 2019).

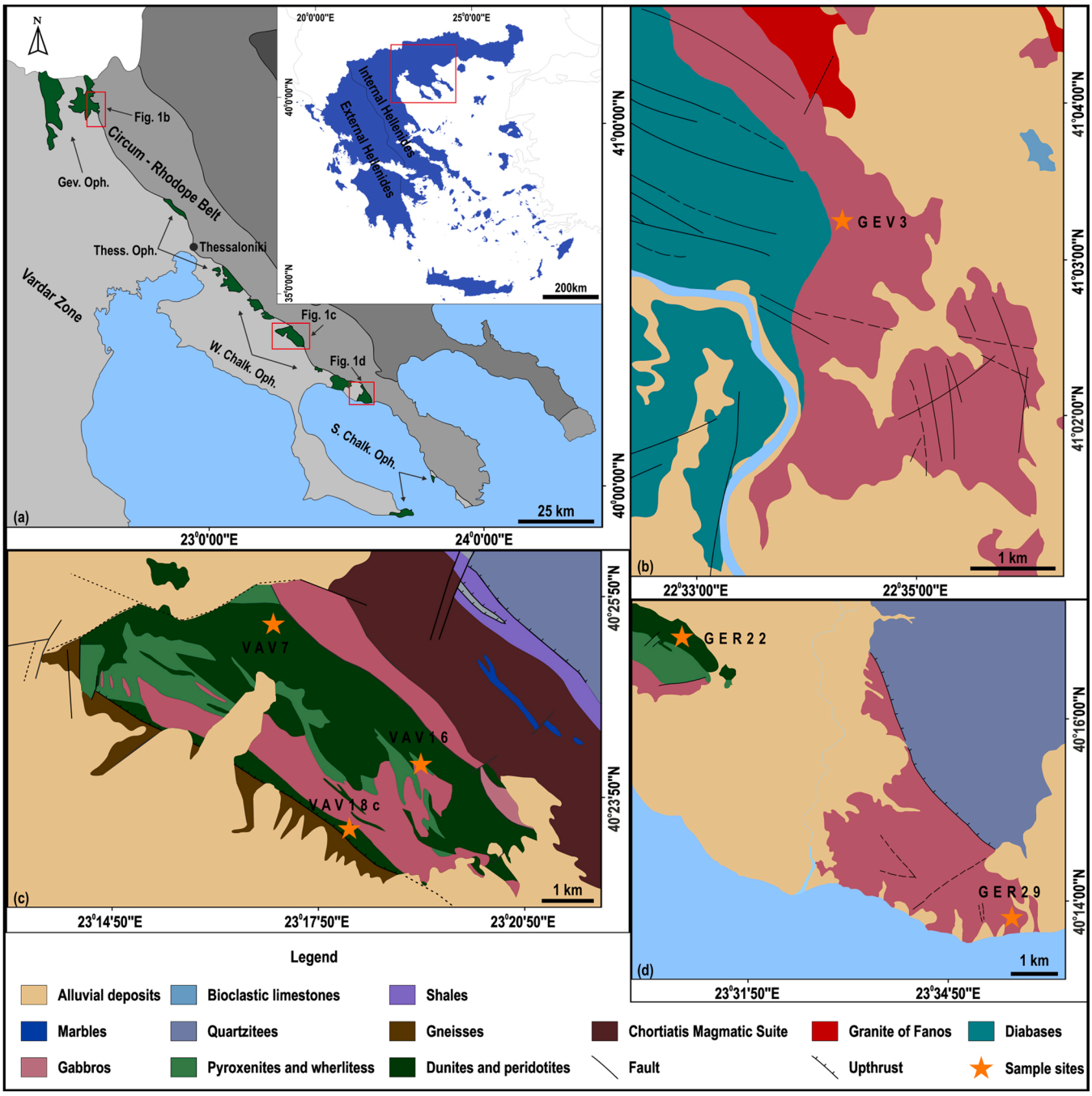

Fig. 1. (a) Simplified Geotectonic map of Central Macedonia (Greece) displaying the main geotectonic zones and ophiolitic units: Gevgelija Complex (Gev. Oph.), Thessaloniki/Oreokastro Units (Thess. Oph.), West Chalkidiki ophiolites (W. Chalk. Oph.) and South Chalkidiki ophiolites (S. Chalk. Oph.). Geological maps of: (b) Gevgelija ophiolite; (c) Vavdos ophiolite; (d) Ormylia and Metamorphosis ophiolites. Geological maps are modified from the 1:50,000 geological sheets of Evzoni, Vasilika, Poliyiros and Arnaea sheets from the Hellenic Survey of Geology and Mineral Exploration (HSGME).

Samples were further petrographically evaluated through other state-of-the-art techniques such as the Quantitative Evaluation of Minerals by Scanning Electron Microscopy (QEMSCAN). Analyses were performed on polished thin sections on an EVO 430 automated scanning electron microscope (SEM) equipped with four light element energy dispersive X-ray spectrometers at the Advanced Mineralogy Facility, SGS Canada. Operating conditions were 25 kV accelerating voltage and with a 5 nA beam current. The processing of both data and images was conducted using iDiscover software package.

X-ray diffraction (XRD) analyses were performed using a Bruker D8 ADVANCE diffractometer, at the Research Laboratory of Rocks and Minerals (UoP), as well as with a Siemens D500 X-ray diffractometer, at the laboratories of the Center for Research and Technology, Hellas (CERTH) in Ptolemais. Operation conditions for both cases were as follows: a CuKα source, accelerating voltage of 40 kV, beam current of 40 mA, 2θ angles from 2° to 70°, with a scanning angle step size of 0.015° and a time step of 0.1 s. Data was processed using DIFFRACplus. Minerals were identified with reference to the powder diffractometry database PDF-2 (ICDD) using the Bruker EVA software (version 5.1). Subsequently, modal composition was quantified using TOPAS software (version 4.2) based on the Rietveld method refinement routine.

Mineral chemistry analyses were performed using a JEOL JSM-6300 scanning electron microscopes, equipped with an energy dispersive spectrometer (EDS) at the Laboratory of Electron Microscopy and

Table 1
Modal composition estimations of the investigated rock samples.

Method		Point counting	QEMSCAN	XRD	MINSQ	AVG	1σ	%CV	μCT
Rock type/Sample name	Mineral								
Gabbronorite/ GER29	Pl	52.4	51.2	47.9	48.7	50.1	2.1	4.2	51.1
	Cpx	22.1	20.4	20.9	22.9	21.6	1.1	5.3	21.4
	Opx	23.6	21.7	27.1	25.5	24.5	2.3	9.6	22.8
	Opq	–	0.1	1.2	1.0	0.8	0.6	76.4	1.0
	Amp	1.9	3.8	2.9	1.9	2.6	0.9	34.8	3.7
Hornblende gabbro/ GEV3	Pl	49.6	48.9	49.5	47.3	48.8	1.1	2.2	52.0
	Mhb	48.4	48.0	46.7	48.9	48.0	0.9	2.0	45.4
	Opq	2.0	2.1	3.8	3.8	2.9	1.0	34.6	2.6
Wehrlite/ VAV16	Ol	49.7	48.0	49.9	47.3	48.7	1.3	2.6	50.6
	Cpx	36.9	34.6	39.1	38.7	37.3	2.1	5.5	33.0
	Opx	2.1	3.1	2.2	1.9	2.3	0.5	22.9	2.5
	Spl	–	0.2	–	0.2	0.2	0.0	0.0	0.1
	Srp	10.4	10.1	7.1	11.6	9.8	1.9	19.5	9.3
	Amp	0.9	3.6	1.7	–	2.1	1.4	67.1	4.6
	Chl	–	0.2	–	0.2	0.2	0.0	0.0	–
	Tlc	–	0.1	–	0.1	0.1	0.0	0.0	–
Harzburgite/ VAV7	Ol	74.8	72.1	70.7	71.0	72.2	1.9	2.6	69.4
	Cpx	0.9	1.3	–	1.0	1.1	0.2	19.5	1.1
	Opx	19.4	18.5	23.5	22.6	21.0	2.4	11.5	23.7
	Spl	0.2	0.6	–	0.4	0.4	0.2	50.0	0.6
	Srp	4.7	6.1	5.8	4.7	5.3	0.7	13.7	5.2
	Tlc	–	0.4	–	0.3	0.4	0.1	20.2	–
Serpentinizeddunite/ GER22	Ol	39.6	38.3	39.5	40.8	39.6	1.0	2.6	38.1
	Cpx	–	0.1	–	0.1	0.1	0.0	0.0	0.2
	Opx	0.2	1.3	1.2	0.7	0.9	0.5	59.6	2.1
	Spl	0.8	1.2	1.2	1.5	1.2	0.3	24.4	1.1
	Srp	40.5	39.8	41.5	38.4	40.1	1.3	3.3	40.0
	Amp	–	0.6	–	1.7	1.2	0.8	67.6	–
	Chl	–	0.3	–	0.3	0.3	0.0	0.0	–
	Cb	18.9	18.2	16.6	16.5	17.6	1.2	6.8	18.5
Semi-massive chromitite/ VAV18C	Spl	54.8	54.2	54.7	56.8	55.1	1.1	2.1	55.1
	Chl	45.2	45.7	45.3	43.2	44.9	1.1	2.5	44.9

Notes: Results obtained through 2D methods (point counting and QEMSCAN) refer to mineral's area (%) in thin sections, whereas results of 3D methods (XRD, MINSQ and μCT) indicate mineral's volume (%). QEMSCAN analyses present total < 100% since through this particular technique have been quantified minor amounts of other accessory mineral phases. These include serpentine, talc and chlorite for the gabbronorite (2.8% in total), chlorite and apatite for the hornblende gabbro (1.0% in total), carbonates for the wehrlite (0.1%), amphibole, chlorite, carbonates and Fe-oxides (opaque) for the harzburgite (1.0% in total) as well as Fe-oxides both for the serpentinized dunite and the chromitite (0.2% and 0.1% in total respectively). Mineral abbreviations based on Whitney and Evans (2010): amphibole of secondary origin (Amp), carbonate mineral (Cb), chlorite (Chl), clinopyroxene (Cpx), magnesio-hornblende (Mhb), olivine (Ol), opaque mineral (Opq), orthopyroxene (Opx), plagioclase (Pl), serpentine (Srp), spinel group mineral (Spl), Talc (Tlc). The error for the XRD is ± 1%, and for all the other techniques is ± 0.5%.

Microanalysis (LEMM) of the University of Patras (UoP), and at the laboratories of CERTH in Thessaloniki. Operation conditions: accelerating voltage of 20 kV, beam current of 0.5 nA and a 2.0 μm beam diameter, total counting time 60 s, detection limits ~0.1%.

Whole-rock analyses were carried out at Bureau Veritas Minerals (BVM) in Canada with the use of ICP–ES. Detection limits range between 0.01 and 0.1 wt% for the major oxides, with accuracy of analyses being within limits of 2–5%. Structural water was removed from sample powders by heating at 1000 °C for 1 h. Mineral chemistry and whole-rock analyses (Tables 2 and 3 respectively; §4.2) were deployed for modal composition quantification through the computational method MINSQ (Herrmann and Berry, 2002).

3.2. X-ray micro-computed tomography

Rock samples considered for X-ray micro-computed tomography were cut into cuboid (~1,5 cm edge) or cylindrical (~2.5 cm diameter, ~3.0 cm height) slabs. All samples were analyzed at the ENAC Platform for X-ray micro-tomography (PIXE) of the Swiss Federal Institute of Technology in Lausanne (EPFL). Analyses were performed on an X-ray micro-CT scanner (Ultratom, RX-Solutions). A Hamamatsu high power X-ray tube was used in reflexion mode with a 0.2 mm thick copper filter and a tungsten target. The acquisition was performed on each sample in cone beam mode with a current of 121 μA and a voltage of 100 kV. During volume data acquisition, the rock samples were rotated by 360 degrees and 1632 projections were taken by steps of ~0.22° to ensure a very precise volume reconstruction. The X-ray beam attenuation was registered by an XL Varian 2530 plane detector with 2176 × 1792 pixels. The projections were then processed (X-act RX-Solutions, filtered backprojection) to reconstruct a corrected volume composed of around 1500 slices in 16-bit Tiff format with an isometric voxel dimension of ~12 μm (maximum resolution), although the best observed resolution was at ~40 μm diameter of grains. Following the suggestions of Aerden and Ruiz-Fuentes (2020), the initial image sequence of CT slices was converted from 16-bit to 8-bit grayscale Tiff; RGB values (0–255), using the open-source Java image processing program ImageJ (Schindelin et al., 2012). Images were then processed with AVIZO v. 2019.4 (FEI, 2019). After image filtering (Avizo, Non-Local Means Filter function), major rock components were segmented by intensity thresholding.

Grayscale intensities of the studied samples were calibrated between the backscattered electron (BSE) images from the scanning electron microscope, with those from the X-ray micro-CT scanner following calibration guidelines with other analogous studies (Pankhurst et al., 2018; Reyes et al., 2017). To determine the grayscale value distribution for each specific mineral, we performed EDS-analyses upon a randomly selected side (outer) of the μCT-scanned cuboid slabs with the use of scanning electron microscope facility. More specifically, every mineral was identified through numerous of microchemical analyses (~50 points for each major phase; ~20 for accessory phases), to locate the specific mineral grains on the BSE image output. The grayscale values of these identified grains were determined with the use of the open-source Java image processing program ImageJ (Schindelin et al., 2012), for

Table 2
Mineral chemistry analyses of participating mineral phases.

	Olivine				Clinopyroxene				Orthopyroxene			
	Wh	Hz	Dn		Gab. Nor.	Wh	Hz	Dn	Gab. Nor.	Wh	Hz	Dn
n	6	12	9		18	5	3	2	8	3	5	3
SiO_2	41.66	40.74	42.47		53.13	53.24	54.48	56.02	54.88	56.84	57.89	56.82
1σ	0.42	0.74	0.50		0.24	0.50	0.44	0.16	0.08	0.22	0.15	1.11
TiO_2	0.06	0.00	0.06		0.10	0.25	0.01	0.10	0.14	0.08	0.04	0.25
1σ	0.07	0.00	0.11		0.03	0.19	0.02	0.13	0.04	0.09	0.07	0.08
Al_2O_3	0.07	0.00	0.03		2.10	2.68	1.24	1.21	1.64	1.14	1.41	0.54
1σ	0.12	0.00	0.06		0.43	0.26	0.13	0.22	0.26	0.27	0.25	0.47
FeO	11.44	9.01	10.00		5.94	2.56	2.24	2.09	13.55	9.06	6.01	6.80
1σ	0.47	0.19	0.50		0.42	0.32	0.29	0.09	0.38	0.48	0.46	0.18
MnO	0.16	0.07	0.19		0.11	0.27	0.09	0.00	0.15	0.27	0.09	0.11
1σ	0.19	0.10	0.15		0.02	0.06	0.07	0.00	0.02	0.17	0.13	0.10
MgO	46.46	50.01	46.21		16.65	15.37	16.10	23.50	28.53	31.28	32.44	33.71
1σ	0.53	0.77	0.54		0.24	0.44	0.29	0.33	0.13	0.65	0.25	2.39
CaO	0.06	0.02	0.08		21.37	24.02	24.53	15.70	0.89	0.35	1.04	0.54
1σ	0.05	0.02	0.10		0.44	0.47	0.41	0.62	0.15	0.25	0.27	0.42
Na_2O	0.00	0.00	0.14		0.08	0.00	0.14	0.14	0.05	0.02	0.02	0.12
1σ	0.00	0.00	0.11		0.03	0.00	0.13	0.19	0.02	0.01	0.03	0.09
K_2O	0.00	0.00	0.02		0.00	0.00	0.03	0.07	0.00	0.02	0.02	0.05
1σ	0.00	0.00	0.04		0.00	0.00	0.02	0.09	0.00	0.01	0.01	0.04
Cr_2O_3	0.02	0.02	0.07		0.09	1.05	0.80	0.35	0.07	0.29	0.71	0.40
1σ	0.04	0.02	0.09		0.03	0.26	0.10	0.08	0.03	0.16	0.23	0.27
NiO	0.11	0.36	0.45		0.05	0.03	0.11	0.15	0.05	0.03	0.11	0.14
1σ	0.13	0.04	0.27		0.01	0.06	0.15	0.21	0.02	0.01	0.14	0.14
Mg#	87.86	90.82	89.18		83.34	91.44	92.76	95.27	78.97	86.01	90.59	89.81
1σ	0.53	0.22	0.55		1.14	1.07	0.78	0.13	0.52	0.89	0.70	0.41
Mineral members												
Fo	87.72	90.76	88.99	En	47.03	43.08	44.6	63.24	77.81	82.42	83.81	89.33
1σ	0.55	0.26	0.52	1σ	0.58	1.37	0.99	0.30	0.30	1.35	0.62	8.02
Fa	12.12	9.17	10.80	Wo	43.37	48.38	48.84	30.36	1.74	0.67	1.94	1.03
1σ	0.54	0.23	0.55	1σ	0.75	0.96	1.22	1.75	0.30	0.47	0.50	0.78
				Fs	9.60	8.54	6.56	6.40	20.45	16.91	14.25	9.64
				1σ	1.12	1.32	1.82	2.05	0.46	0.90	0.63	7.25

	Plagioclase		Amphibole	Spinel group			
	Gab. Nor.	Horn. Gab.	Horn. Gab.	Wh	Hz	Dn	Chrom
n	22	10	11	2	18	2	20
SiO_2	45.54	56.47	47.25	0.00	0.06	0.03	0.00
1σ	0.29	0.72	0.49	0.00	0.07	0.04	0.00
TiO_2	0.01	0.01	1.18	0.03	0.15	0.14	0.31
1σ	0.01	0.01	0.19	0.01	0.12	0.18	0.09
Al_2O_3	34.60	27.36	7.62	30.31	18.11	11.22	19.31
1σ	0.26	0.55	0.76	0.66	0.43	0.23	0.48
FeO	0.22	0.23	16.34	21.55	21.38	23.53	20.30
1σ	0.02	0.02	0.34	0.44	0.95	0.77	0.45
MnO	0.01	0.01	0.30	0.20	0.34	0.33	0.41
1σ	0.01	0.01	0.09	0.28	0.04	0.47	0.05
MgO	0.02	0.02	11.43	11.40	9.29	6.85	15.12
1σ	0.01	0.01	0.74	1.18	0.61	0.37	0.28
CaO	18.65	9.68	11.60	0.00	0.00	0.00	0.00
1σ	0.16	0.49	0.36	0.00	0.00	0.00	0.00
Na_2O	0.74	6.07	0.91	0.00	0.00	0.00	0.00
1σ	0.04	0.25	0.04	0.00	0.00	0.00	0.00
K_2O	0.02	0.05	0.52	0.00	0.00	0.06	0.00
1σ	0.01	0.02	0.11	0.00	0.00	0.05	0.00
Cr_2O_3	–	–	–	35.49	48.80	56.34	42.67
1σ	–	–	–	1.68	0.70	1.20	0.58
NiO	–	–	–	0.37	0.02	0.22	0.10
1σ	–	–	–	0.52	0.02	0.00	0.04
Mineral members			Mg#	51.91	45.26	35.26	70.36
An	93.20	46.72	1σ	3.89	2.62	1.27	1.13
1σ	0.35	2.25	Fe#	48.09	54.74	64.75	29.64
Ab	6.69	52.98	1σ	3.89	2.62	1.27	1.13
1σ	0.35	2.26	Cr#	43.98	64.38	77.10	59.72
Or	0.11	0.30	1σ	1.70	0.80	0.74	0.85
1σ	0.05	0.11					

Notes: Wh: Wehrlite, Hz: Harzburgite, Dn: serpentinized dunite, Gab. Nor.: Gabbronorite, Horn. Gab.: Hornblende Gabbro, Chrom: Chromitite.

specifying the specific range of grayscale values upon the calculated histogram. Crystals with the highest and lowest grayscale values in the BSE-image were then matched with the corresponding crystals of the μCT slice microphotograph to determine the grayscale value distribution for each mineral phase in the μCT image; these are provided in Table 4 (§5.1).

4. Results

4.1. Petrographic description and modal composition

The gabbroic samples considered (gabbronorite and hornblende microgabbro), predominantly consist of plagioclase and mafic minerals (pyroxene and amphibole). Accessory minerals include Fe-Ti oxides

Table 3
Whole rock major element (wt%) composition of studied ophiolitic mafic and ultramafic rock samples.

Major Element (wt%)	Mafic rock samples		Ultramafic rock samples			
	Gabbronorite	Hornblende gabbro	Wehrlite	Harzburgite	Serpentinizedunite	Chromitite
SiO_2	47.53	48.69	46.22	44.87	34.67	14.31
TiO_2	0.12	1.40	0.04	0.03	0.01	0.16
Al_2O_3	18.09	16.32	1.21	0.42	0.26	17.45
Fe_2O_3	5.99	11.64	6.54	8.49	8.19	16.19
MnO	0.11	0.19	0.10	0.14	0.11	0.17
MgO	12.21	5.46	32.42	43.61	40.64	20.61
CaO	14.81	10.12	11.23	0.51	0.37	0.07
Na_2O	0.29	3.18	0.05	0.02	0.03	0.02
K_2O	0.01	0.47	0.02	0.01	0.03	0.01
Cr_2O_3	0.03	0.02	0.45	0.39	0.91	25.08
NiO	0.02	0.01	0.11	0.31	0.29	0.18
LOI	0.29	1.18	1.28	0.38	12.91	5.62
SUM	99.50	98.68	99.67	99.18	98.42	99.87

Table 4
Calculated μCT grayscale values of the participating mineral phases as determined through the methodology described in §3.2.

Mineral	Mafics				Ultramafics							
	Gab.-nor		Horn.-Gab		Wh		Hz		Dn		Chrom	
	Min	Max	Min	Max	Min	Max	Min	Max	Min	Max	Min	Max
Plagioclase	64	89	75	95	–	–	–	–	–	–	–	–
Carbonates	–	–	–	–	–	–	–	–	80	99	–	–
Serpentine	–	–	–	–	98	157	118	156	100	110	–	–
Amphibole	90	91	96	125	176	176	–	–	–	–	–	–
Chlorite	–	–	–	–	–	–	–	–	–	–	101	140
Clinopyroxene	92	100	–	–	177	216	184	190	180	196	–	–
Orthopyroxene	101	140	–	–	158	159	157	165	111	111	–	–
Olivine	–	–	–	–	160	175	166	183	112	179	–	–
Spinel	–	–	–	–	217	255	191	255	197	255	141	230
Oxides	141	255	126	255	–	–	–	–	–	–	231	255

(magnetite and ilmenite) and apatite, as well as other minor secondary mineral phases (epidote, sericite, chlorite, actinolite). The modal composition was determined by point counting, QEMSCAN, XRD analyses (Fig. 2), MINSQ computational method and X-ray micro-computed tomography (see Table 1). Despite differences, obtained results do not vary highly, as shown by the standard deviations in their average results.

Based on this, the gabbronorite (GER29) contains plagioclase (avg. 50.1 ± 2.1 (± 1σ) vol%), clinopyroxene (avg. 21.6 ± 1.1 (± 1σ) vol%), orthopyroxene (avg. 24.5 ± 2.3 (± 1σ) vol%), whereas other accessory phases and secondary minerals are present in minor amounts (Table 1). Petrographic observations reveal that plagioclase is present in the form of euhedral to subhedral cumulate textured grains (~1.0 mm) and less

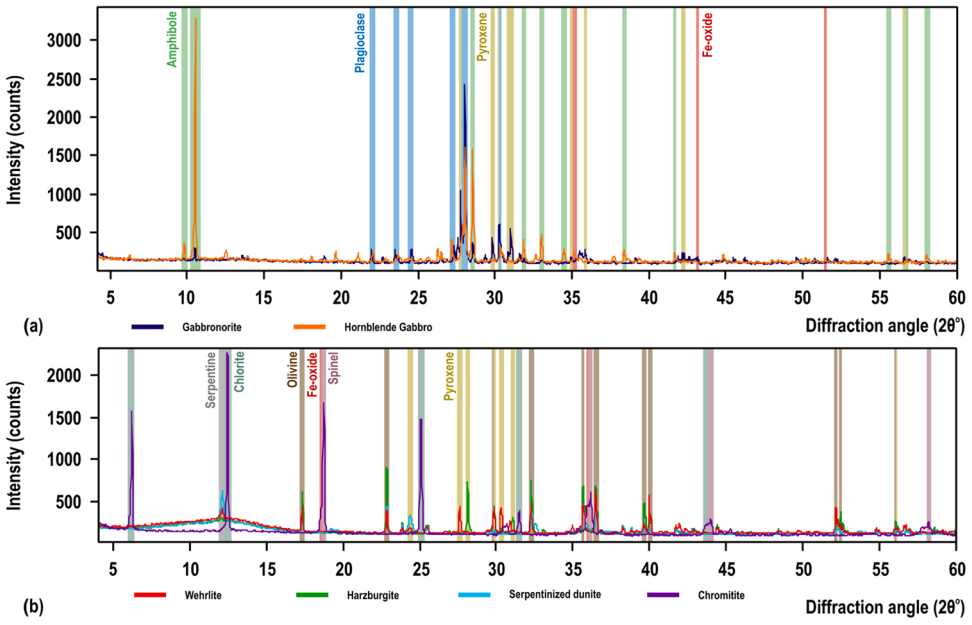

Fig. 2. X-ray diffraction (XRD) profile patterns of mafic rock samples (gabbronorite, hornblende gabbro) and ultramafic rock samples (wehrlite, harzburgite, serpentinized dunite, chromitite) with mineral identification lines. Note that only the major peaks of each mineral phase are highlighted.

often as laths. They encapsulate poikilitic anhedral clinopyroxene and subhedral orthopyroxene grains forming locally ophitic, subophitic and more often granular textures (Figs. 3a, 4a). Clinopyroxene grains are ~0.5 mm in size, whereas orthopyroxene grains are larger in size (up to 1.2 mm). Some of the orthopyroxene grains host clinopyroxene exsolution lamellae. In a few cases, clinopyroxene is partly uralitized at the rims, forming aggregates of secondary fibrous amphibole (actinolite) and minor chlorite. The hornblende microgabbro (GEV3) mainly consists of primary amphibole (magnesio-hornblende) (avg. 48.0 ± 0.9 (± 1σ) vol%) and plagioclase (avg. 48.8 ± 1.1 (± 1σ) vol%) (Table 1). Fe-Ti oxides, as well as secondary sericite appear in smaller amounts (<3.0 and <0.5 vol% respectively). Both hornblende and plagioclase develop subhedral to anhedral grains (avg. size ~0.3 mm and ~0.2 mm respectively) forming subophitic textures (Figs. 3b, 4b). Restricted metasomatism is observed through minor occurrence of chlorite, whereas deformation is imprinted by plagioclase twinning, as well as slight elongation of plagioclase and hornblende.

Examined peridotite samples consist of a wehrlite, a harzburgite and a serpentinized dunite. These rocks also include accessory minerals (spinel group minerals: chromite, magnesiochromite, spinel and Fe-oxides).

The effect of alteration is noted by the presence of serpentine, actinolite, chlorite, carbonates (calcite, dolomite, magnesite) and minor talc. The wehrlite (VAV16) mostly contains olivine (avg. 48.7 ± 1.3 (± 1σ) vol%), clinopyroxene (avg. 37.3 ± 2.1 (± 1σ) vol%) and lesser orthopyroxene (avg. 2.3 ± 0.5 (± 1σ) vol%). Secondary chlorite and talc are present in minor amounts (≤ 0.2 vol%), except for serpentine (avg. 9.8 ± 1.9 (± 1σ) vol%) (Table 1). Coarse-grained olivine (up to

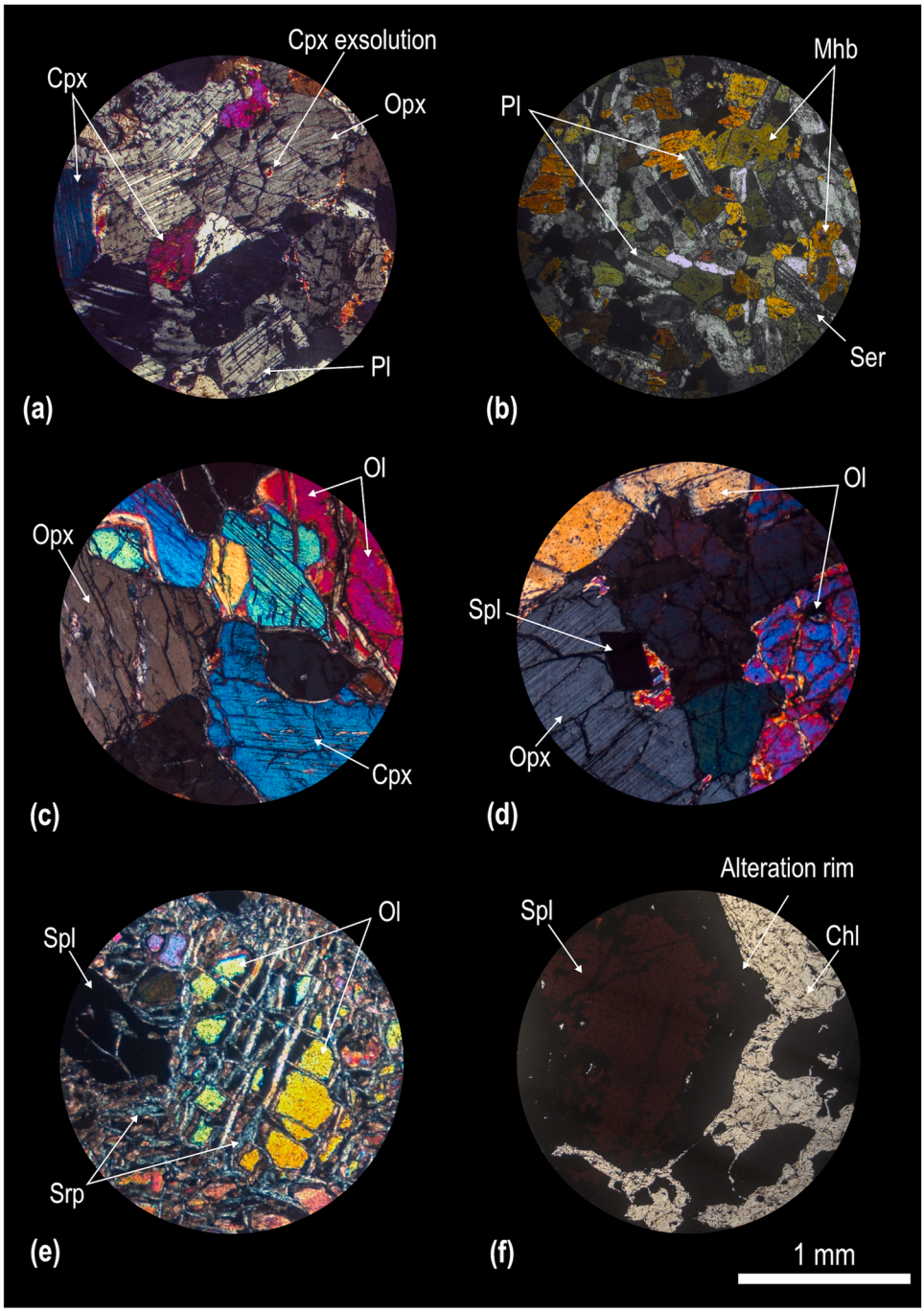

Fig. 3. Photomicrographs obtained from petrographical microscope; (a-e) under cross-polarized light and (f) parallel-polarized light. (a) Gabbronorite; Euhedral plagioclase (Pl) enclosing anhedral clinopyroxene (Cpx) and subhedral orthopyroxene (Opx) grains. Orthopyroxenes host clinopyroxene exsolution lamellae. Actinolite formed at the expense of clinopyroxene grain at the rims. (b) Hornblende gabbro; magnesio-hornblende (Mhb) surrounding subhedral plagioclase laths. Minor sericite (Ser) after alteration of plagioclase. (c) Wehrlite; olivine crystals (Ol) with curvilinear boundaries surrounding subhedral orthopyroxene (Opx) and clinopyroxene (Cpx) grains. (d) Harzburgite; Chromite (Spinel group mineral; Spl) between coarse-grained olivine and orthopyroxene. (e) Serpentinized dunite; Mesh textures of serpentine (Srp) enclosing olivine crystals. (f) Chromitite; Brown to reddish brown magnesiochromite (Spinel group mineral; Spl) with alteration rim developed along with chlorite (Chl) under parallel-polarized light.

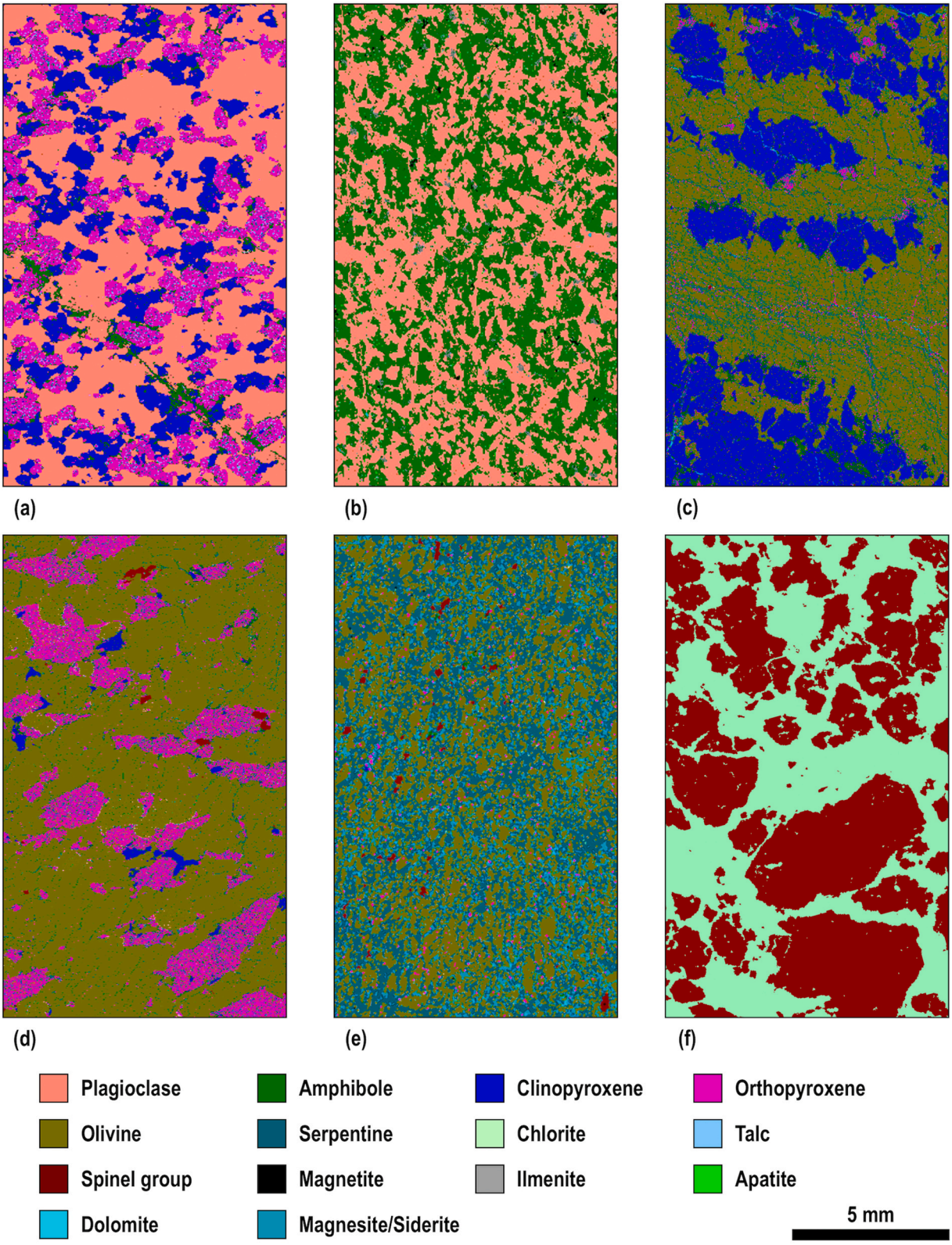

Fig. 4. Pseudo-colored mineralogical images from QEMSCAN analyses. (a) Gabbronorite; plagioclase, clinopyroxene and orthopyroxene grains forming ophitic and subophitic textures. Secondary amphibole (actinolite) rims clinopyroxene and appears as veinlets. Minor serpentine and talc detected within orthopyroxene. (b) Hornblende gabbro; Primary amphibole (magnesio-hornblende) and plagioclase grains forming subophitic textures. (c) Wehrlite; clinopyroxene and olivine grains forming granular textures, along with accessory orthopyroxene. Serpentine fills fractures in olivine grains. (d) Harzburgite; orthopyroxene and olivine grains forming granular textures along with disseminated chromite (Spinel group mineral). (e) Serpentinized dunite; disseminated chromite (Spinel group mineral) and serpentine that surrounds olivine and orthopyroxene display cataclastic textures. (f) Chromitite; coarse-grained magnesiochromite (Spinel group mineral) surrounded by a matrix of chlorite.

3 mm) with curvilinear boundaries is interwoven with smaller subhedral to anhedral clinopyroxene (up to 2.5 mm) forming granular textures (Figs. 3c, 4c). Even though orthopyroxene occurs as an accessory phase, it is present in the form of isolated subhedral to anhedral grains (< 1 mm) and is typically surrounded by olivine. Spinel is fine grained (~0.2 mm), disseminated and mostly enclosed within olivine. Serpentine, minor chlorite, talc and carbonate minerals are present in intragranular microcracks of olivine grains. The harzburgite (VAV7) contains olivine (avg. 72.2 ± 1.9 (± 1σ) vol%) and orthopyroxene (avg. 21.0 ± 2.4 (± 1σ) vol%) with minor clinopyroxene (avg. 1.1 ± 0.2 (± 1σ) vol%) (Table 1). Other mineral phases include accessory chromite along with secondary serpentine (avg. 5.3 ± 0.7 (± 1σ) vol%). Both subround olivine and subangular orthopyroxene are coarse-grained (<4 mm and 3 mm respectively) forming granular textures (Figs. 3d, 4d). Clinopyroxene is present in relatively restricted amounts (Table 1), in the form of subangular to subrounded grains (~1 mm). Chromite grains (<0.6 mm) are disseminated, often occurring at junction points in olivine and orthopyroxene. Serpentine and minor secondary phases (chlorite, talc and carbonates) are present within intragranular microcracks of olivine.

In the serpentinized dunite (GER22), amongst the primary minerals, olivine is the most abundant phase (avg. 39.6 ± 1.0 (± 1σ) vol%), whereas pyroxenes are rare. Metasomatism had a rather significant impact, as noticed by the relatively high participation of serpentine (avg. 40.1 ± 1.3 (± 1σ) vol%) and carbonates (avg. 17.6 ± 1.2 (± 1σ) vol%) (Table 1). Accessory mineral phases are present in small amounts. Fragmented olivine grains (<0.8 mm) are enclosed by mesh serpentine (Figs. 3e, 4e) and are occasionally cross-cut by sparse chrysotilic veinlets. Serpentine has replaced olivine and orthopyroxene grains (bastites), whereas microcrystalline carbonates represent the late-stage metasomatic phase. Subrounded and disseminated chromite (<1 mm) is also present. The semi-massive chromitite sample (VAV18C) is predominantly comprised of magnesiochromite (avg. 55.1 ± 1.1 (± 1σ) vol%), and interstitial chlorite (avg. 44.9 ± 1.1 (± 1σ) vol%; Table 1). Magnesiochromite appears as subangular grains (≤5 mm), which are rimmed by secondary ferrirchromite and are fractured forming pull-apart textures (Figs. 3f, 4f).

4.2. Mineral chemistry

The studied peridotites include forsterite-rich olivine grains: wehrlite (avg. $Fo_{87.72}$), harzburgite (avg. $Fo_{90.76}$) and serpentinized dunite (avg. $Fo_{88.99}$) (Table 2). The slightly lower forsterite contents of olivine in the wehrlite are assigned to the cumulate nature of the rock. Their MnO, CaO and Cr_2O_3 contents are generally low (<0.2 wt%), whereas NiO contents are low for those present within the wehrlite (avg. 0.11 wt %) and slightly enhanced for olivine in the harzburgite and serpentinized dunite samples (avg. 0.36 and 0.45 wt% respectively). Rims of olivine grains in the serpentinized dunite display higher Fe amounts compared to their cores, a feature attributed to serpentinization.

Following the IMA nomenclature of Morimoto (1988), clinopyroxene in the gabbronorite is classified as augite (avg. $En_{47.03}Fs_{9.60}Wo_{43.37}$). The Mg# values (Mg# = [Mg/(Mg + Fe) x 100]) of clinopyroxene grains present within gabbronorite are rather high (Table 2), whereas the CaO, Al_2O_3 and TiO_2 contents can be considered as moderate (avg. 21.37, 2.10 and 0.10 wt% respectively). Wehrlite and harzburgite comprise of clinopyroxene classified as diopside (avg. $En_{43.08}Fs_{8.54}Wo_{48.38}$ and $En_{44.60}Fs_{6.56}Wo_{48.84}$ respectively). These are characterized by high Mg# values along with high CaO contents (avg. 24.02 and 24.53 wt% respectively). On the other hand, Al_2O_3 and FeO contents in diopsides are higher for those present within the wehrlite (avg. 2.68 and 2.56 wt% respectively) compared to those within the harzburgite (avg. 1.24 and 2.24 wt% respectively). Microanalyses of orthopyroxene grains within both gabbronorite and peridotite samples correspond to enstatite. The composition of enstatite differentiates between the gabbronorite (avg. $En_{77.81}Fs_{20.45}Wo_{1.74}$), wehrlite (avg. $En_{82.42}Fs_{16.91}Wo_{0.67}$) and harzburgite (avg. $En_{83.81}Fs_{14.25}Wo_{1.94}$). Their Mg# values can be considered as being slightly low in the gabbronorite, moderate in the wehrlite and relatively high in the harzburgite (Table 2). In addition, their Al_2O_3 contents in all samples are relatively low (avg. 1.64, 1.14 and 1.41 wt% respectively).

Spinel grains within the wehrlite display moderate Mg# and Cr# values (Cr# = [Cr/(Cr + Al) × 100]). The latter is assigned to the rather balanced Cr_2O_3 and Al_2O_3 contents (avg. 35.49 and 30.31 wt% respectively). Spinel group minerals of both harzburgite and serpentinized dunite are classified as chromite (Cr-spinel) displaying rather low Mg# and high Cr# values (Table 2). Grains of spinel group minerals within the chromitite sample are classified as magnesiochromites; their TiO_2 contents are overall low (avg. 0.31%) corresponding to those typically found in ophiolitic/podiform chromitites.

Regarding the feldspars, gabbronorite mainly comprises of anorthitic plagioclase (avg. $An_{93.2}$), whereas the hornblende gabbro mainly includes andesitic plagioclase (avg. $An_{46.7}$), along with albite (avg. $An_{5.0}$), oligoclase (avg. $An_{12.8}$) and labradorite (avg. $An_{54.0}$) (Table 2). Amphibole in the same sample is magnesio-hornblende, with rather high Al_2O_3, Na_2O and TiO_2 contents (avg. 7.62, 0.91 and 1.18 wt% respectively), likely assigned to magmatic rather than metamorphic origin (Gillis, 1996; Koutsovitis and Magganas, 2016; Tribuzio et al., 2000).

4.3. Micro-computed tomography

The μCT was applied on the six selected mafic and ultramafic samples. In the gabbroic samples, plagioclase phase was easily distinguished from clinopyroxene, orthopyroxene and amphibole. In the 3D projections, the plagioclase grains are interwoven with these minerals and in some cases encapsulate them (Figs. 5a, 5b). However, differentiating between the mafic minerals presents difficulties mostly attributed to their similar attenuation coefficient properties (see §5.1). Accessory minerals (Fe-Ti oxides) are exclusively hosted within orthopyroxene, displaying either bleb-like textures. In the hornblende gabbro, magnetite and ilmenite are present as inclusions in hornblende. The Fe-Ti oxides are relatively larger compared to those within the gabbronorite.

The three ultramafic rock samples (wehrlite, harzburgite, serpentinized dunite) along with the semi-massive chromitite were considered as appropriate for conducting μCT since these rocks comprise of at least one major mafic mineral component that include clinopyroxene, orthopyroxene, olivine and spinel group minerals. Discrimination between these Mg-Fe silicate mineral phases presented similar challenges with those encountered for the gabbroic mafic minerals and thus similar methodologies were applied to distinguish them. In the wehrlite, olivine develops granular to porphyroclastic textures and in most cases encloses clinopyroxene subhedral cluster grains or less frequently porphyroclasts (Fig. 5c). Similarly, in the harzburgite olivine surrounds slightly deformed medium-grained orthopyroxene phenocrysts, although some appear as fine-grained crystals (Fig. 5d). Despite their textural similarities, in the μCT, orthopyroxene is more easily distinguished from olivine than in the case of clinopyroxene from olivine. Spinel and serpentine were effectively recognized from other Mg-Fe silicate phases, due to their considerable density differences. With the three-dimensional reconstruction, it was observed that clinopyroxene voxels within wehrlite are slightly elongated locally forming clusters, whereas in the harzburgite the orthopyroxene voxels are short and prismatic, dispersing through olivine. Spinel within wehrlite is typically small-sized and scattered forming bleb-like textures of relatively high sphericity and low angularity properties, whereas chromite in the harzburgite is relatively larger in size displaying irregular shapes with rather low sphericity and moderate angularity properties. Dunite was subjected to more extensive serpentinization processes compared with the other two ultramafic samples considered, with the three main constituents (olivine, serpentine and chromite) in the μCT images being easily visually distinguished. Relict olivine appears either as isolated grains or forming clusters surrounded and crosscut by replacive serpentine

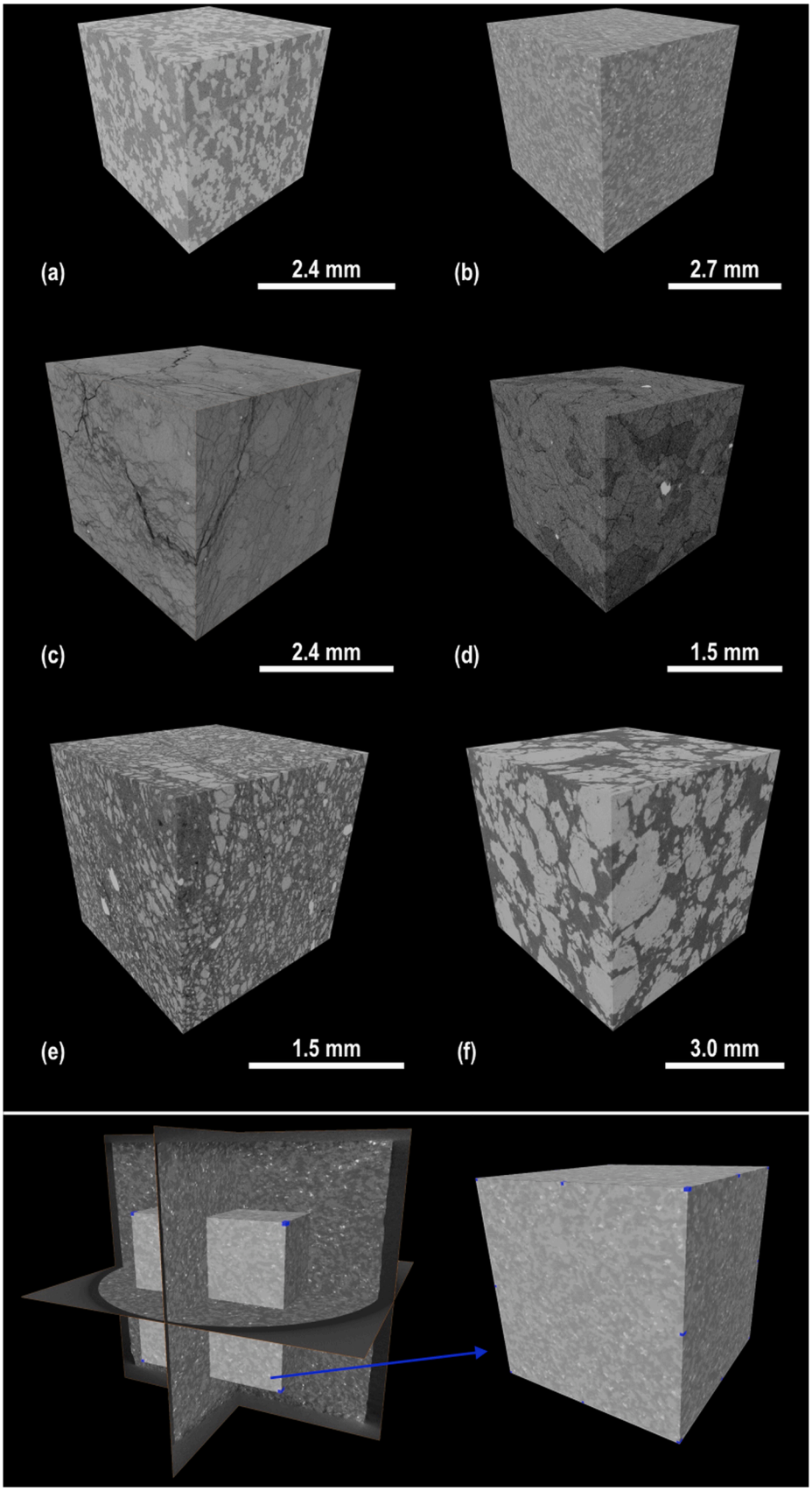

Fig. 5. Visualization of rock samples scanned by X-ray μCT. (a) Gabbronorite; Highly interconnected grains of plagioclase (dark gray) surrounding pyroxene grains (light gray). (b) Hornblende gabbro; Plagioclase (dark gray) subophitically enclosing hornblende grains (light gray), along with minor Fe-Ti oxides (lightest gray). (c) Wehrlite; Serpentine veins (darkest gray) cutting mainly through olivine (dark gray) and clinopyroxene (light gray) grains. Very fine-grained spinels (lightest gray) are scattered through sample. (d) Harzburgite; Orthopyroxene grains (dark gray) surrounded by olivine (light gray) developing porphyroclastic textures. Irregular shaped chromite grains (lightest gray) are easily detected along with crosscutting serpentine (darkest gray). (e) Serpentinized dunite; Relict olivine grains (light gray) and chromite grains (lightest gray) present through serpentine (darkest gray). (f) Semi-massive chromitite; magnesiochromite grains (light gray) within chlorite matrix (dark gray). Below the white line is presented on the left side the volume rendering of the hornblende gabbro (26.62 × 27.83 × 25.71 mm) along with the three orthoslices and on the right side an occurred cubic sub-volume (13.6 × 13.6 × 13.6 mm) as an example of the process followed for the visualization of all samples (a)-(e).

(Fig. 5e). In the 3D projection, most of the olivine and spinel crystals are characterized by moderate sphericity and relatively low angularity properties. In the semi-massive chromitite sample, magnesiochromite and chlorite were also efficiently distinguished due to their significant density contrasts (Fig. 5f). Magnesiochromite grains (Cr-ore) disperse throughout the chlorite matrix and in some cases are fractured into finer crystals forming small clusters.

5. Discussion

5.1. Effectiveness of μCT upon ophiolitic rocks

An increasing number of geological research studies deploy X-ray micro–Computed Tomography (μCT) to investigate and determine the mineralogical properties of natural rock samples, although unexplored research aspects remain (Carlson, 2006; Carlson et al., 2003; Cnudde and Boone, 2013; Ketcham and Carlson, 2001; Noiriel, 2015). Despite these efforts there are still some drawbacks with the applicability of this technique that are mainly related with data processing and the necessity of combining results with other analytical methods (Guntoro et al., 2019). Godel (2013) noted the importance of a detailed petrographic study (e.g. crystal's zoning, deformation patterns, alteration) along with a good knowledge of the mineral chemistry prior to deploying other state-of-the-art techniques. The μCT has been proven to provide clear visualization constraints when performed upon altered rocks, including serpentinites and carbonated ultramafic rocks such as listvenites and ophicalcites (Beinlich et al., 2020; Maurício et al., 2017; Noël et al., 2018; Okazaki et al., 2021), as well as metasomatized xenoliths (Howarth et al., 2015; Patkó et al., 2020). The study of relatively unaltered ultramafic rocks, such as wehrlites and harzburgites or mafic gabbroic through μCT presents additional challenges. This is attributed to the fact that the participating mineral phases may present similar attenuation coefficient and/or density properties. This is displayed in their grayscale values, which fluctuate between upper and lower values,

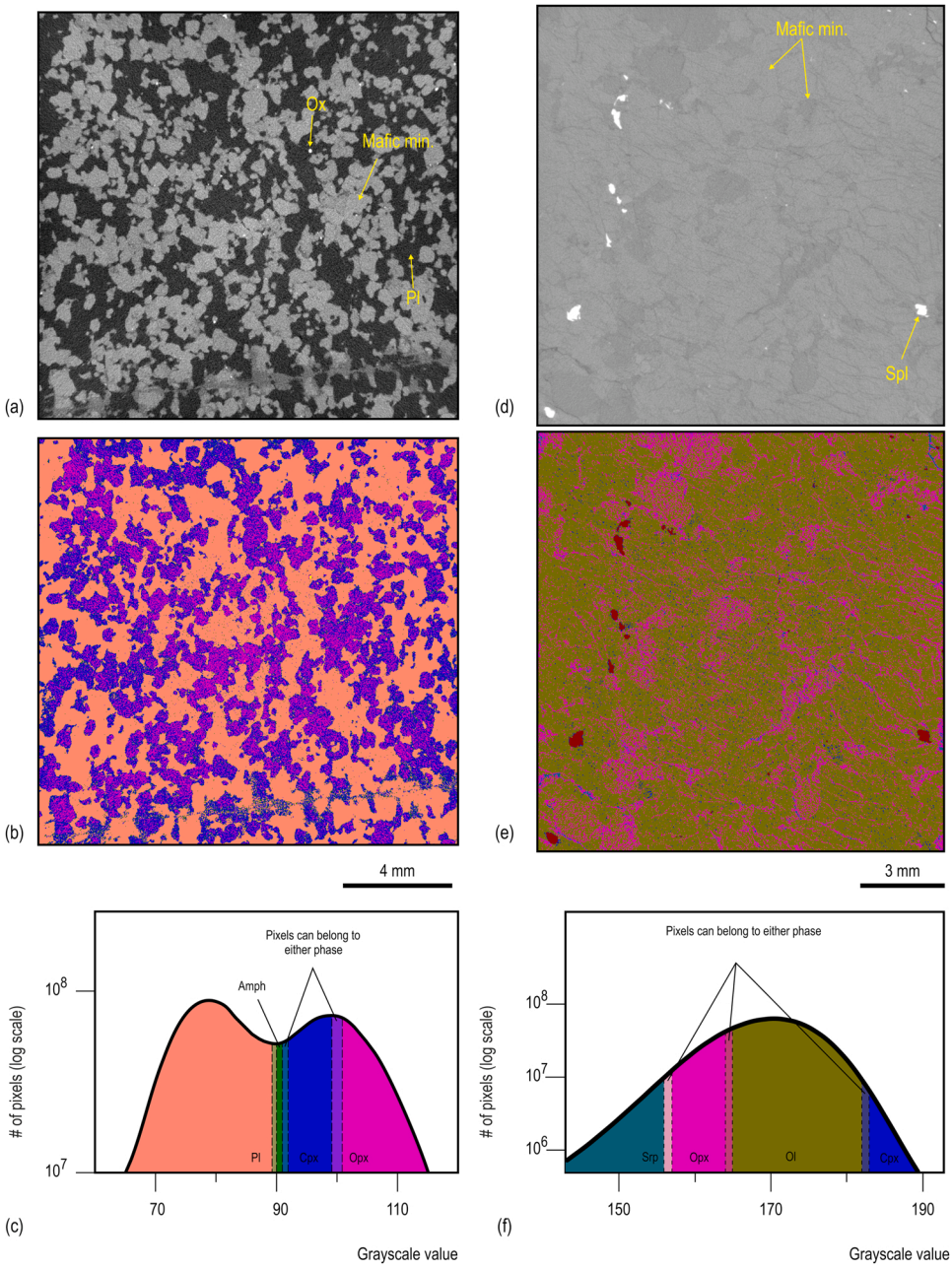

Fig. 6. Segmentation of the participating mineral phases through samples' subvolume. Gray scale image of 2D slice and psedo-colored image after segmentation based on mineral's gray scale values of gabbronorite sample (a), (b) and harzburgite (d), (e) respectively. Mafic min.: mafic mineral (i.e., clinopyroxene, orthopyroxene, olivine), Ox: Fe-Ti oxides, Pl: plagioclase, Spl: spinel. Histogram of gray scale values (0–255) showing limits between plagioclase, amphibole (Amp), clinopyroxene (Cpx) and orthopyroxene (Opx) for gabbronorite sample (c) and serpentine (Serp), orthopyroxene, olivine (Ol) and clinopyroxene for harzburgite sample (f).

a feature related to the distinct chemistry of each mineral (Pankhurst et al., 2014; Tsuchiyama et al., 2000; Uesugi et al., 2010).

Discrimination between plagioclase and mafic minerals with the use of μCT alone was evidently observed (e.g., see Figs. 6a, 6b), whereas distinction amongst the individual mafic mineral phases (e.g., clinopyroxene, orthopyroxene and/or olivine) was not apparent (Figs. 6d, 6e). To distinguish amongst participating mineral phases, various image segmentation methods along with several software algorithms have been applied for processing μCT data that include: histogram analysis, thresholding, region based and watershed methods (Aerden and Ruiz-Fuentes, 2020; Bhanot et al., 2020; Godel, 2013; Jerram et al., 2010; Miller et al., 2016; Porfido et al., 2020; Reyes et al., 2017; Uesugi et al., 2010; Zucali et al., 2014). To obtain sufficient results for the studied samples, histogram analysis and thresholding methods were combined (Fig. 6c, 6f), after BSE image processing (see §3.2), that have been obtained of SEM-EDS facility. Modal composition results obtained from deploying this methodology are listed in Table 1 (§4.1), which are highly comparable with results derived through other conventional techniques listed. In particular, the μCT results fall within the calculated 1σ range of average results from the aforementioned techniques.

In the gabbroic samples, plagioclase grains exhibit restricted distributions in their calculated grayscale index values (Table 4), which is attributed to their distinct mineral chemistry: CaO and Al_2O_3 average contents of plagioclase is respectively: 18.65 and 34.60 wt% in the gabbronorite, 9.68 and 27.36 wt% in the hornblende gabbro (see Table 4). Anorthitic plagioclase grains within the gabbronorite display a distribution of grayscale values ranging between 64 and 89, whereas andesine within hornblende gabbro ranges between 75 and 95. The observed anorthic plagioclase grayscale distributions of the gabbronorite are highly comparable with those reported by Gawrońska et al. (2019) for compositionally similar plagioclase from the Apollo 15 pigeonite basalt (sample 15085), ranging between 66 and 82. Amphibole grains within the gabbroic samples present different but close-range distributions (Table 4). This is also associated with differences in their mineral chemistry that highly depend on the origin of the amphiboles (magmatic or metasomatic). Amongst the mafic phases, the hornblende gabbro comprises almost exclusively of magmatic hornblende (with high FeO and Al_2O_3), exhibiting a wider range of grayscale values compared with that of actinolite in the gabbronorite. The latter appears at the rims of clinopyroxene and presents comparable grayscale values with the lower ones of clinopyroxene. Mineral chemistry is not the only factor that contributes to the x-ray attenuation within a natural rock sample; e.g. their scalability may be affected by mineral impurities, zoning and alteration (Ketcham, 2005a), although these features were not often identified in the samples of our study suite. However, the distribution of the grayscale values seems to be influenced by their mineral modal composition and by their coexistence with other mineral phases resulting in the "partial volume effect" that broadens the grayscale index values in the outputted CT images (Godinho et al., 2019; Kuper et al., 2007; Pankhurst et al., 2018; Wang and Miller, 2020). The distribution of pyroxene's grayscale values differs between mafic and ultramafic rock samples participating in variable amounts; these may either be predominant or accessory phases. According to Howarth et al. (2018), the basaltic shergottite martian meteorite NWA 8657 that comprises of pigeonite and augite clinopyroxene, displays grayscale index values ranging between 70 and 140 (Porfido et al., 2020). Augite clinopyroxene grains within the compositionally comparable gabbronorite from our study suite fall within this range (grayscale index values 92–100; Table 4). On the other hand, ultramafic samples comprise of diopside clinopyroxene, with higher grayscale values (177–216 and 184–190 for the wehrlite and harzburgite respectively; Table 4), signifying the importance of predetermining the nature and composition of the rocks considered. Although clinopyroxene CT values do not strongly rely upon their Mg# values (Tsuchiyama et al., 2000), the Mg# of augite and diopside present within our studied samples exhibit rather noticeable differences (Table 2) that likely had an impact on the distribution of CT values (Table 4). However, it seems probable that these were mostly influenced by the fact that these minerals appear within rocks that exhibit variability in their mineralogical properties (predominance of non-mafic plagioclase or mafic olivine) and thus coexist with other mineral phases that tend to display distinct X-ray attenuation properties. This feature can also be noticed when comparing the lunar basalt sample 15085 (Gawrońska et al., 2019) with the martian basaltic meteorite sample NWA 8657 (Porfido et al., 2020), which both predominantly comprise of clinopyroxene but coexist with compositionally different plagioclase-related phases. In particular, in each of these samples, clinopyroxene CT values exhibit a rather moderate distribution (83–110 and 70–140 of the aforementioned respectively) likely attributed to different the X-ray attenuation properties of the coexisting mineral phases that strongly rely on the mineral's X-ray attenuation values and to a lesser extent from their chemistry properties.

On the other hand, the CT distribution values of diopside grains present within the wehrlite and harzburgite are in close range, which is attributed to the fact that they are both hosted within compositionally comparable ultramafic rocks, as well by their highly comparable mineral chemistry properties (Avg. Mg# 91.44 and 92.76 for diopside in the wehrlite and the harzburgite respectively; Table 2). Differences in their grain size and participation in dissimilar amounts do not seem to have a significant impact on the distribution of their grayscale index values. On the contrary, despite the fact that orthopyroxene in all studied samples compositionally corresponds to enstatite, their Mg# values vary significantly (Avg. 78.97, 86.01 and 90.59 for the gabbronorite, wehrlite, harzburgite respectively). This variability significantly affects the distribution of grayscale index values (Table 4), a feature which has been noted by Tsuchiyama et al. (2000). Enstatite grains present in the gabbronorite display grayscale values ranging between 101 and 140, whereas in the ultramafic samples they are slightly higher (157–165). Ultramafic samples differ from the mafic, since the former host relatively high amounts of olivine (see Table 1; §4.1) and display grayscale values that reside between orthopyroxene and clinopyroxene. Olivine grayscale values for wehrlite and harzburgite are highly comparable, ranging tightly between 160 and 183, whereas olivine in serpentinized dunite displays a broader range (112–179; Table 4). An important factor that contributed to the latter feature is its relatively high exposure to the effects of serpentinization compared to the other ultramafic samples (relatively high LOI; Table 3).

Mineral chemistry analyses performed upon olivine grains in the serpentinized dunite revealed higher Fe amounts of rims compared to cores, a feature not noticed for olivine in the other ultramafic rocks. This is attributed to serpentinization and to the relatively small grain size of the residual olivine. Tsuchiyama et al. (2000) noted the significance of changes in Fe contents of olivine in the distribution of CT values, which does not seem to be highly influential for pyroxenes. Serpentine's grayscale distribution values of wehrlite and harzburgite are also highly comparable, ranging highly between 98 and 157, whereas serpentine in the serpentinized dunite ranges tightly between 100 and 110 (Table 4). This seems to be attributed to the fact that in the first case serpentine polymorphs of the ultramafics are either lizardite or chrysotile, whereas in the serpentinized dunite they are predominantly lizardite. An alternative interpretation may be the crystallinity of serpentine; in its first stages (low alteration degrees) serpentine or 'proto-serpentine' demonstrates a chrysotile-range order (Lafay et al., 2016) forming embryonic porous crystals mixed with brucite (Lafay et al., 2016; Peuble et al., 2018). Well-developed phases will eventually be produced in more advance metasomatic stages. Furthermore, the chemistry of the serpentine and iron uptake could also have a significant role, since serpentinized dunite is composed mainly of Fo-rich olivine serpentine will be Mg-rich, whereas for the formation of serpentine in the cases of the rest of peridotites, orthopyroxene and less forsteritic olivine can contribute resulting in heterogeneities in the final serpentine chemistry and subsequently in its grayscale distribution. Another factor that likely contributed to this characteristic is the fact that serpentinization in the

dunite affected only olivine and not additionally pyroxenes as in the case of the other ultramafics (see Fig. 3; §4.1). Within the serpentinized dunite, the carbonate alteration mineral phases present even lower CT values (89–99) compared to those of lizardite serpentine. The distribution of spinel group mineral CT values presents within most ultramafic rocks (wehrlite, harzburgite, serpentinized dunite) is relatively constant, ranging between 191 and 255 (Table 4). The coexistence of magnesiochromite grains within a chlorite-rich matrix in the chromitite sample mainly accounts for the observed shift to lower grayscale index values (141–230), assigned to the partial volume effect (Kuper et al., 2007), although alteration of the magnesiochromite rims (see Fig. 3; §4.1) likely contributed to the rather expanded distribution of the aforementioned values. It should be noted that magnesiochromite is a major mineral constituent in the chromitite and not an accessory phase, as noticed for spinels in the other ultramafics, coexisting with chlorite that displays significantly lower CT values (101–140).

5.2. 3D rock fabric analysis

Fabric analysis of natural rocks, including textural and structural information of mineral phases, conducted through μCT, can shed light regarding their mineral properties in three dimensions, apart from the mineral volumetric portions. However, a precise and detailed mineral characterization is a prerequisite for achieving optimum data processing of micro-computed tomographic results. This allows to perform advanced 3D investigations focusing on aspects such as mineral's grain growth during magmatic crystallization, foliation and lineation (Chatzaras et al., 2016; Kahl et al., 2017; Mote et al., 2010), as well as to identify crystal orientation or stretching of phenocrysts resulting from deformation related to metamorphic processes (Ketcham, 2005b; Sayab et al., 2017). An increasing number of publications (Aerden et al., 2021; Corti et al., 2019; Dilissen et al., 2021; Sayab et al., 2021) have combined μCT results with geotectonic and microtectonic data to determine deformation markers, development of newly formed metamorphic minerals and to conduct fabric analysis. X-ray μCT has also been applied to mantle-related ultramafic rocks mainly focusing on the study of peridotite xenoliths to unravel mechanisms associated with lithospheric modification and delamination (Bhanot et al., 2017, 2020; Chatzaras et al., 2016). On the other hand, ophiolitic rocks are often affected by deformation, related with their emplacement through exhumation and overthrusting at the stage of oceanic closure (Dijkstra et al., 2002; Rassios and Moores, 2006). Conventional structural micro-tectonic methodologies have been used to determine these mechanisms; e.g. in mantle ophiolitic rocks in Othris (Greece) these reveal the mantle shear zone deformation patterns mostly by combining two-dimensional thin section observation and analysis coupled with geochemical data (Dijkstra et al., 2002).

In cases of well-defined deformation patterns, mineral phases tend to develop orientated fabrics, which can be measured from an orientated 2D thin section parallel to the lineation and perpendicular to the foliation, which is easily predetermined even with an unaided eye. Although even in the highly foliated rock samples the vast majority of mineral's major axis follows the main lineation trend, some of the crystals may be aligned in random directions from the preferable tendency, which are often not easily distinguished in thin sections. An additional factor that may further affect the orientation of crystals is the likeliness of rocks to be affected by two distinct or more deformation events resulting different major axis orientations. Thin sections display a distinct two-dimensional perspective, which may not be sufficient for conducting in-depth fabric analysis upon fairly deformed ophiolitic rocks with a preferable but not prominent orientation trend. Besides, measurement's reliability should be considered taking into account the randomness of the obtained thin section in three-dimensions within the sample considered. The recourse for three-dimensional examination through microscopy (optical and/or electronic) requires significant amount of two-dimensional perspective data that often deploy either time-consuming serial sectioning or sample's carving both supervening partly damage or even entire destruction of the rock sample. Such difficulties can be met and overcome with the use of μCT, since a rock volume is investigated through a non-destructive manner and subsequently the analyses conducted can provide continuous information (see §5.3) for all participating grains referred in three-dimensions (Popov et al., 2020). Therefore, identification even in case of slightly imprinted deformation patterns is attainable though 3D ellipsoidal measurements. Aside from orientation data, three-dimensional analyses provide other important shape property information such as circularity and sphericity of the participating mineral phases.

In order to identify the applicability of μCT 3D measurements in determining geotectonic related deformation parameters in ophiolitic rocks, two examples of 3D rock fabric analysis from relatively unaltered mafic and ultramafic samples are presented (hornblende microgabbro and harzburgite samples). The harzburgite comprises of weakly elongated orthopyroxene, whereas restricted deformation has been identified in magnesiohornblende within the hornblende gabbro. Samples were initially processed using Blob3D software (Ketcham, 2005a), in which principal measurements of participating mineral's voxels in each rock sample (volume and shape measurements) were calculated after mineral segmentation and separation. Following this procedure, results were then evaluated by implementing the open-source TomoFab MATLAB code (Petri et al., 2020), which takes advantage of directional cosines and lengths of the three axes defined by the individual best-fit ellipsoid in order to perform fabric analysis.

In fabric diagrams, plagioclase grains present within hornblende gabbro are predominately clustered exhibiting preferentially linear crystals (Fig. 7a). As defined by the linear fabric tensor after standardization (see Petri et al., 2020), best-fit ellipsoids are prolate ellipsoids (rod-shaped) that are characterized by a rather high shape parameter ($T = -0.94$) and moderate anisotropy ($P' = 1.45$), corresponding to the relatively ideal crystal shape of plagioclase grains. Their volume exhibits an extended distribution (1.52–9.86 mm^3), due to significant interconnection amongst single plagioclase grains, confirmed from petrographic observations (see Figs. 3, 4; §4.1). The continuous network of aggregated grains generally leads to larger ellipsoid volumes. On the contrary, magnesiohornblende grains within same sample are preferentially plano-linear, displaying smaller ellipsoid's volumes that are delimited between 0.01 and 0.77 mm^3 (Fig. 7b). Although few individual ellipsoids are scattered, most appear clustered, which according to the linear fabric tensor ($T = -0.02$; $P' = 1.23$) form almost neutral ellipsoids. Orientation data obtained by the ellipsoids are projected to equal area low hemisphere (Schmidt net) with a referenced frame for each sample. Selected plagioclase grains present girdle distribution with almost N and S point maxima, whereas minor axis (V_3) draws a horizontal moderate girdle distribution that dips to the SE, in which a point distribution to the W can also be noticed (Fig. 8a).

V_1 axis of ellipsoids corresponding to magnesiohornblende similarly display a girdle distribution with N and S point maxima, whereas V_3 axis exhibits a clear vertical point distribution (Fig. 8b). On the other hand, best-fit ellipsoids calculated for orthopyroxene present within the harzburgite are preferentially linear to almost pano-linear (Fig. 7c). Their shape matches prolate to neutral ellipsoids ($T = -0.15$; $P' = 1.08$) and their volume ranges between 0.10 and 0.75 mm^3. It should be noted that these shape and volume properties correspond to orthopyroxene subgrains whose boundaries are defined even from small-scale discontinuities (e.g., micro-cracks, restricted alteration zones) observed through conventional petrographic methods (see Figs. 3, 4; §4.1). The harzburgite sample can serve in this aspect as an excellent example for evaluating size and/or orientation data, processed through μCT for the participating mineral phases, in case where microcracks are deployed. The orientation of the orthopyroxene subgrains does not display a specific pattern for V_1 axis, whereas V_3 axis exhibits a clear vertical point distribution (Fig. 8c). The best-fit ellipses of the chromite voxels within the harzburgite are preferentially planar to pano-linear occupying

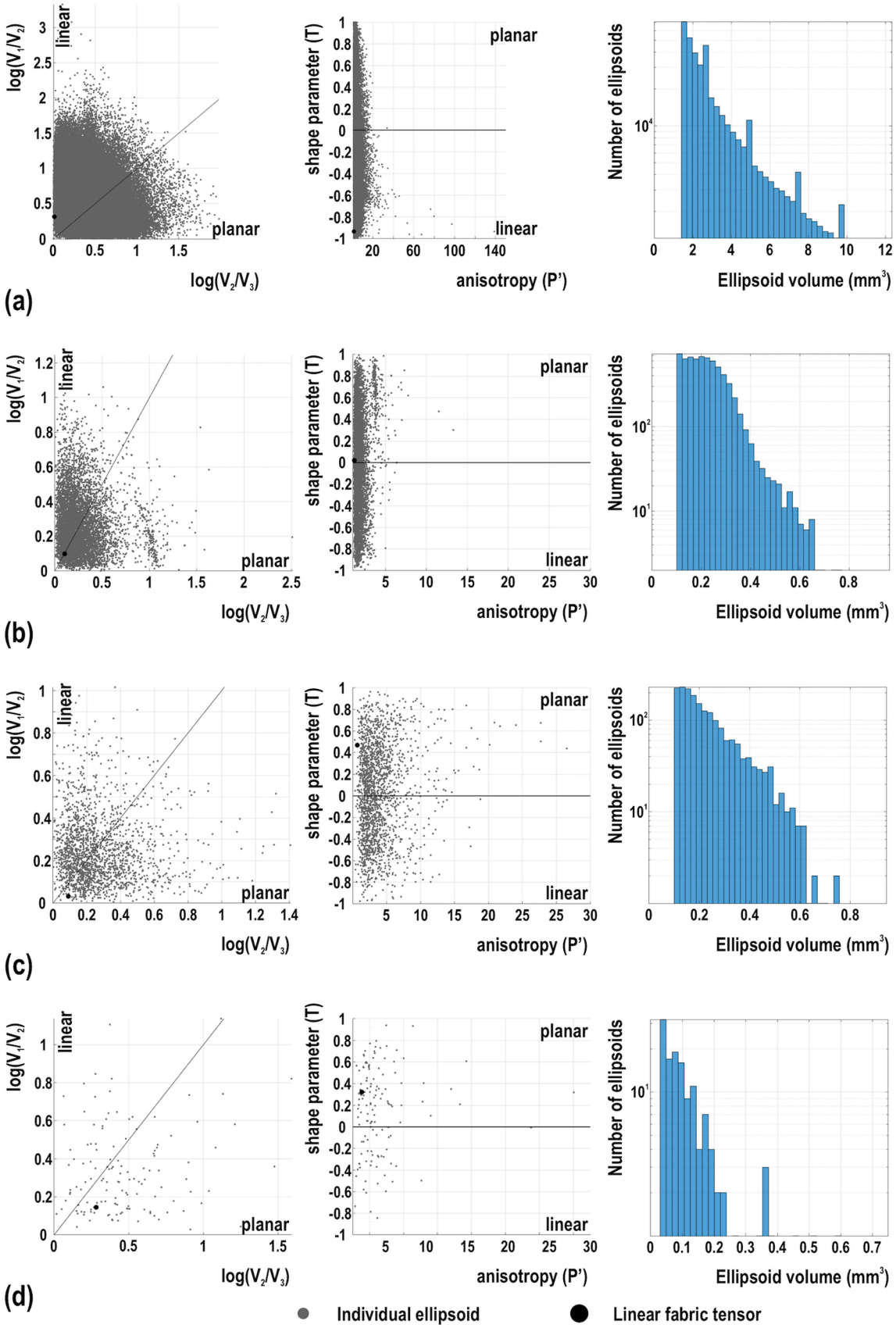

Fig. 7. Fabric diagrams of mineral's best-fit ellipsoids and corresponding bar charts of their volumes; Mafic hornblende gabbro sample with (a) plagioclase grains, (b) magnesiohornblende grains and for the ultramafic harzburgite sample with (c) orthopyroxene grains, (d) chromite grains. Graphs use a log base 10 scale.

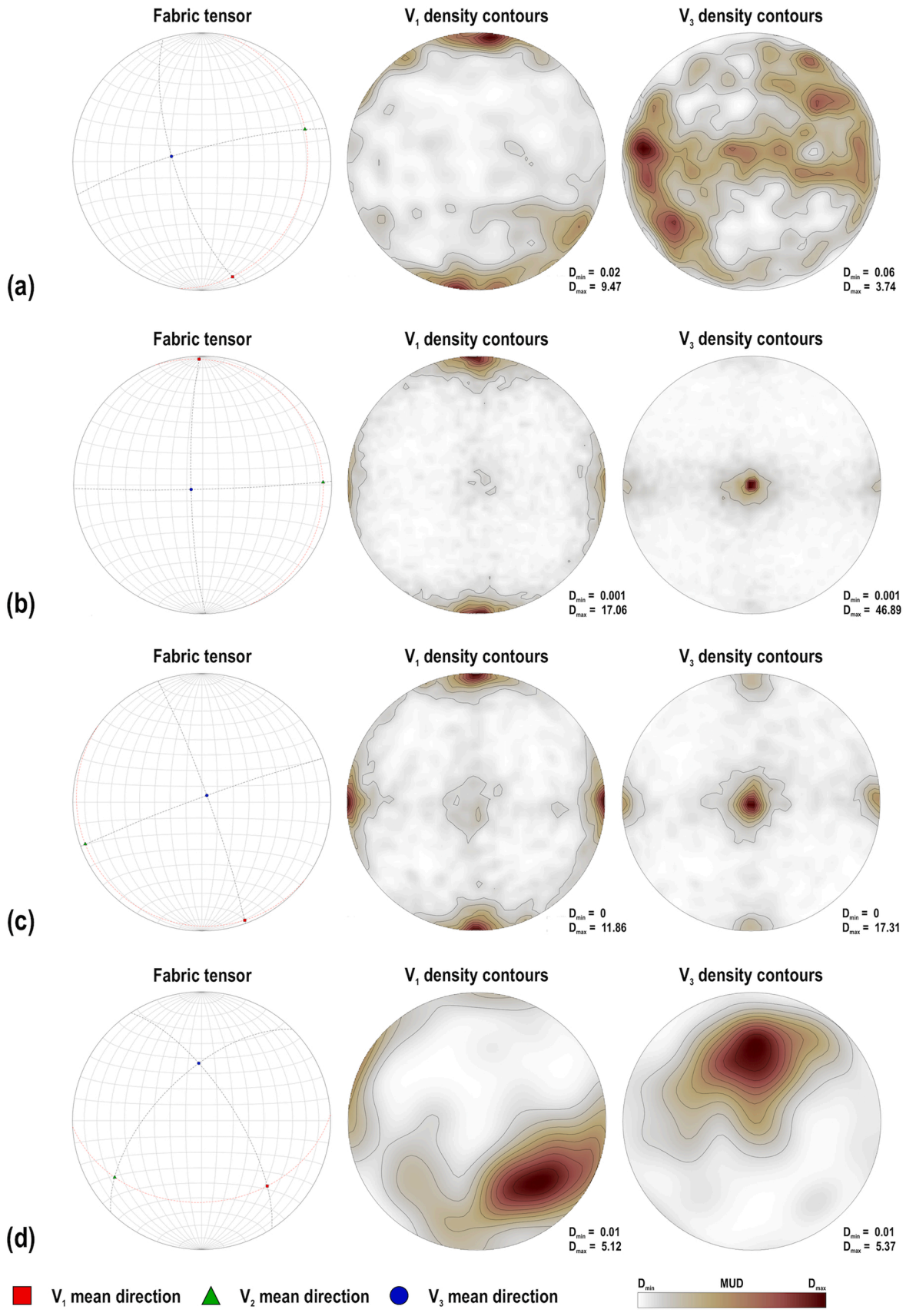

Fig. 8. Linear fabric tensor calculated by orientation distribution of mineral's best-fit ellipsoids and orientation density contour maps of ellipsoid's major (V1) and minor (V3) axes; Mafic hornblende gabbro sample with (a) selected plagioclase grains, (b) magnesiohornblende grains and for the ultramafic harzburgite sample with (c) orthopyroxene grains, (d) chromite grains Orientation data (equal area lower hemisphere spherical projection) are in sample reference frame. Density contour maps are represented in multiples of uniform distribution (MUD). Graphs use a log base 10 scale.

volumes that range between 0.03 and 0.59 mm^3 (Fig. 7d). Based on the calculated linear fabric tensor (T = 0.32; P′= 1.55), they can be classified as oblate ellipsoids (disk shaped). Projected orientation data of ellipsoids as shown in Fig. 8d, exhibit girdle distribution for major axis (V_1) with NNW and SSE point maxima, as well as a clear point distribution for minor axis (V_3). Tensor shape parameters of mineral phases, as determined from their linear fabric tensors based on individual best-fit ellipsoids respectively, indicate a slight deformation impact upon the mafic hornblende gabbro sample and a rather moderate to low impact upon the ultramafic harzburgite sample.

5.3. *Combined techniques for optimum characterization of ophiolitic rocks*

To achieve the most precise characterization of individual rock samples, researchers have focused their efforts in deploying various methodologies so as to obtain the maximum possible information. In order to identify the mineral constituents and textural features of ophiolitic rock samples it is required to conduct a thorough and detailed petrographic examination of thin section slices. Further examination requires determination of the modal composition quantification though standard point counting technique that can be applied either manually or with specific ancillary devices. The modal composition is calculated considering the proportion of each participating mineral phase based upon the occupied area of the 2D section. Despite the development of various software applications such as GeoPixelCounter (Mock et al., 2012), Rock.AR (Larrea et al., 2014), and JMicroVision (Roduit, 2019), petrographic point counting still remains a procedure that requires considerable user's knowledge in the field of petrography and mineralogy to precisely identify the proportional participation of mineral phases. Accuracy is highly related with the grid of points considered and should be carefully selected tacking into consideration the grain size of the minerals presents within the investigated rock. On the other hand, X-ray Diffraction (XRD) technique is used to obtain a rough estimation regarding the nature of the participating minerals and their modal composition (Rietveld quantitative analysis; (Bish and Post, 1993)). It is an alternative that can either stand alone or used as an ancillary method when mineral identification and modal composition quantification are not applicable through optical/electron microscopy. Although the results obtained are semi-quantitative, the XRD technique when applied in ophiolitic rocks poses the advantage of distinguishing amongst the different serpentine polymorphs (e.g., lizardite, antigorite, chrysotile). It should be noted that quantification may present limitations in cases where mineral phases participate in relatively minor amounts.

Determining modal composition percentages through point counting techniques is often combined either with electron microscopy coupled with mineral chemistry analysis (EM) to serve for obtaining detailed mineralogical and petrological research objectives, or with X-ray diffraction analysis (XRD) for adequate petrological/geological assessments or for geoengineering related purposes (Method 1; Fig. 9). Combination of the aforementioned techniques leads to a conventional characterization that is sufficient for identifying mineral phases, determining their participating percentage and individual chemistry, as well as for determining the suitability of the ophiolitic rocks to be considered for further scientific research purposes (e.g. study of the lithospheric mantle, magma processes, geodynamic implications) or to determine their suitability for applied research purposes such as their usage as aggregates (e.g., concrete, railway ballast, road construction, pavement structures) or for CO_2 mineralization applications (Đokić et al., 2020; Fournari et al., 2021; Giannakopoulou et al., 2018; Kelektsoglou, 2018; Koukouzas et al., 2019; Lampropoulou et al., 2020; Magganas and Koutsovitis, 2015; Petrounias et al., 2018; Pomonis et al., 2007; Rogkala et al., 2019). By deploying XRD through Method 1, mineral identification and petrological assessments can be achieved, also providing the additional advantage of unraveling the presence of various polymorphs, and also to identify accessory mineral phases that may be anisotropically present within the rock sample and which may not appear within a randomly chosen 2D thin section slice.

To obtain even more precise quantification of the mineral modal compositions of the examined ophiolitic rocks compared to the convectional point counting technique, we proceeded in applying QEMSCAN analyses that permit fully automated and rapid measurements (Hoal et al., 2009). QEMSCAN is typically used in the mining industry to assess beneficiation of various ore types and to apply the

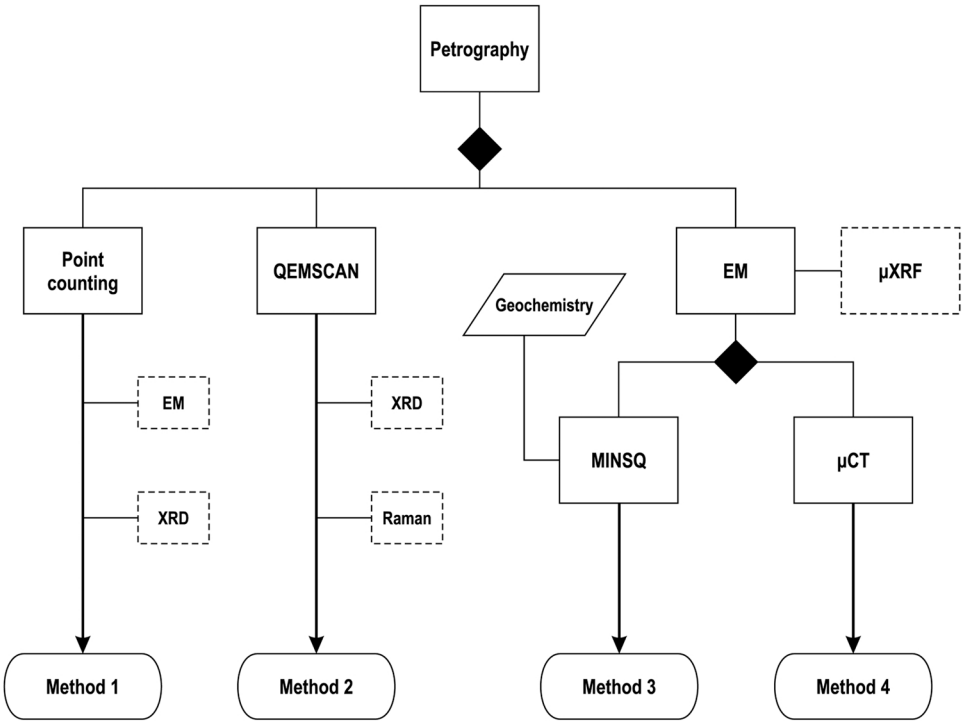

Fig. 9. Workflow of common techniques and proposed methods combining them for applying upon investigating ophiolitic rocks samples. Dashed rectangles present optional techniques that can be deployed in each proposed method. Techniques' *abbreviations*: Electron microscopy coupled with mineral chemistry analyses (EM); Scanning Electron Microscope with Energy Dispersive Spectroscopy (SEM/EDS) or with Wavelength Dispersive Spectroscopy (SEM/WDS) and Electron probe micro analyzer (EPMA), Raman Spectroscopy (Raman), X-Ray Diffraction (XRD) and micro–X-Ray Fluorescence (μXRF).

appropriate metallurgical approach to extract for example PGM (platinum-group minerals) from Cr-ores (Pascoe et al., 2007; Tripathy et al., 2019) or other precious/critical rare and base metals (e.g., Au, Cu, Ni) from relevant deposits (Godel, 2013; Warlo et al., 2019). Phase assemblage maps were produced from the investigated thin sections (Fig. 4; §4.1), in which each pixel represents both energy-dispersive X-ray spectra and backscattered-electron (BSE) image information (Gottlieb et al., 2000). These assemblage maps project the participating mineral phases after having been automatically identified within a database of mineral species, based on their chemical composition along with BSE brightness at each measurement point. Although modal composition results are obtained significantly faster along with their mineral characterization, petrography is a prerequisite step that was performed upon the investigated samples to avoid any mineral misidentification amongst the participating phases. QEMSCAN can be complied with XRD (Method 2; Fig. 9) for discriminating different polymorphs similar to Method 1. This methodology provides better insights for ophiolitic rocks that were subjected to rather moderate alteration processes (Miller et al., 2017; Tominaga et al., 2021). In cases that secondary processes leads to the development of non-common phases, it is suggested to additionally deploy Raman spectroscopy to reveal their presence and distribution (Mayhew et al., 2018). Samples considered in our study suite were not significantly affected by alteration, which was evidently revealed by the QEMSCAN results (Fig. 4). The serpentinized dunite and the chromitite samples did not require further investigation with additional techniques, since petrographic results (apart from calcite and chlorite respectively) did not reveal other important secondary phases.

The modal composition of ophiolitic rocks can be further estimated and/or confirmed by applying the MINSQ computational methodology (Tilhac et al., 2016; Yu et al., 2014). The accuracy of the results highly depends on precision of the whole-rock and mineral chemistry data obtained. Application of Method 3 (Fig. 9) can provide robust results in cases that the number of mineral phases is rather limited; thus, this is not suggested when ophiolitic rocks have been subjected to extensive alteration processes. Compared to this method, Method 2 can provide further insights regarding the extent and nature of alteration, as well as the related textural features, although Method 3 can be mainly used for the purpose of lithological classification complimentary to petrography. In cases that the petrographic examination reveals participation of many mineral phases (including serpentine polymorphs), Method 3 can be combined with Method 1 for more accurate results (Lu et al., 2011), provided that all participating phases have been recognized and chemically analyzed with the application of electron microscopy facility.

Although the aforementioned methods provide information regarding the participating minerals, as well as the modal composition quantification, these are calculated based upon either 2D petrographic thin sections or from analyses performed on powdered rock volumes; either through XRD facility (Methods 1 and 2) or by applying the MINSQ software (Method 3). These methods (1–3) remain in a static two-dimensional perspective regarding the textural properties, as well as the preferred orientation of the participating minerals. In order to examine samples in a three-dimensional perspective though microscopy (optical and/or electronic), it is required to include a large number of two-dimensional data either through serial sectioning or sample's carving, both of which result in the partial or complete damage of the rock sample (Peuble et al., 2018; Yan et al., 2017). This information can be better achieved by utilizing the X-ray micro–Computed Tomography technique through Method 4 (Fig. 9). Apart from obtaining information regarding textural properties (size, shape, roughness) and structural data (distribution, orientation), modal composition quantification through μCT may be more representative since it refers to a rock volume of specified dimensions and is implemented through a non-destructive manner. Compared with the conventual techniques that are applied either upon petrographic thin sections or crushed powders, μCT processes the ability to provide continuous image data information without boundaries between each individual slice (Fig. 10). Methods that

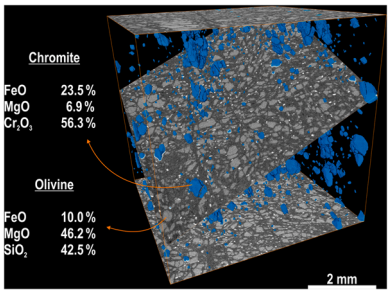

Fig. 10. Schematic illustration presenting the stereological error phenomenon in which the investigated slice and its randomness within a cuboid slab of a rock sample; showing here the example of chromite (spinel group mineral) with blue color within the serpentinized dunite. Note that both bottom and top planes are perpendicular to z axis. The random plane which typically use conventional two-dimensional methods can vary extremely in three-dimensions effecting modal composition, textural and shape features as well as grain's size and any preferable mineral orientation.

necessarily require the deployment of petrographic thin sections present some drawbacks, since the examined thin section slice is often randomly selected. Taking into account that rocks are by definition solid materials, a randomly directional slice may not be quite representative regarding the proportion of the participating mineral phases and their properties (known as stereological bias phenomenon; (Lätti and Adair, 2001; Sutherland, 2007)), such as grain size distribution, grain's orientation; if existing, interfacial area, shape features and textural information (Miller and Lin, 2004). The study conducted by Militello et al. (2019), which examines the phases of asbestos minerals, is an exceptional example of the advantages presented by Method 4 compared to Methods 1–3 regarding the textural investigation of the initial features within the rock sample examined, underlying the morphological influence as a result of sample's comminution. μXRF can also be regarded as an additional technique or even a non-destructive alternative for EM to determine the mineral's elemental composition when required (Bergqvist et al., 2019; Porfido et al., 2020; Suuronen and Sayab, 2018; Wildenschild and Sheppard, 2013). Although Method 4 possess many advantages, the deployment of EM along with μCT is strongly suggested as their integration is beneficial for investigating rock's mineral constituents (De Boever et al., 2015). Similar conclusions have been drawn by Warlo et al. (2021) after combining EM with X-ray computed tomography although this concerns ore characterization. This mostly applies in this study to ultramafic (e.g., lherzolite, harzburgite) and mafic (e.g., gabbronorite) rock samples that comprise of more than one mafic mineral constituent (e.g., olivine, clinopyroxene, orthopyroxene). However, hornblende gabbro that is characterized by the participation of only one mafic mineral phase, can be effectively analyzed without the necessity of EM related facilities.

From this point of view, X-ray micro–Computed Tomography opens new perspectives in the fields of petrography for both scientific and applied research purposes. The application of this technique upon ophiolitic rocks, but also of other natural rock samples, is evolving into a necessary tool to precisely determine modal compositions of participating mineral phases, textural features, mineral interactions, grain sizes and their preferable orientation in a three-dimensional perspective. Furthermore, results obtained through μCT can further be exploited for conducting advanced analyses (see §5.2). This information can be applied to resolve complex petrological and petrogenetic issues regarding the magmatic crystallization processes, evaluation of solid, melt and fluid inclusions, permeability and their relationships with magmatic and post-magmatic processes (Bhanot et al., 2020; Godel et al., 2013; Gomila et al., 2019, 2021; Okazaki et al., 2021; Parisatto et al., 2018; Patkó et al., 2020; Prichard et al., 2017, 2018, 2015; Richard et al., 2019). Deformation patterns can be more easily recognized upon ophiolitic rocks or other examined natural rock samples (Liu

and Dai, 2021; Milatz et al., 2021; Yang et al., 2017) since there is the asset of examining individually each grain size of the participating mineral phases tacking principal measurements for their shape. In addition, orientation data can correlate with separate grain size groups, evaluating not only the preferred orientation but also examining whether these groups present orientation and their intensity. Likewise, the mobility of alteration-related fluids that result in serpentinization or carbonation of ophiolitic rocks can be reconstructed for computed modeling purposes to determine the kinetics of the newly formed secondary minerals (Prodanović et al., 2015).

It is evident that 3D information can be also beneficial for conceptionally resolving geomechanically related problematics, in which mineral orientation is a critical parameter; in case of rock slopes where mineral's preferred orientation can affect the stability since mafic ophiolitic rocks are often excavated (Gomila et al., 2021). The major utility of ophiolitic rocks typically concerns aggregates in several application, thus, mineral constituents and their 3D arrangement could also be important for aggregate's suitability as they can affect their physicomechanical properties or proved to be hazard for public heath when containing asbestos mineral phases. In addition, this approach can significantly contribute to the success of the widely discussed and urgent problematic that concerns CO_2 storage. The obtained 3D information is a necessary basis for precisely examining and determining the petrophysical parameters of ophiolitic rock formations that are considered as candidates for deploying CO_2 capture and storage techniques (Carbon Capture and Storage - CCUS) through mineral carbonation (Snæbjörnsdóttir et al., 2020) or through porous lithotypes such as basalts or sandstones (Callow et al., 2018; Uemura et al., 2011; Voltolini et al., 2017), since the μCT can identify the microporous internal structure that is associated with critical parameters that include permeability and the specific area of the mineral.

6. Conclusions

X-ray micro-computed tomography (μCT) was applied upon selected ophiolitic rock samples from various localities of the Vardar ophiolite outcrops in North Greece, in order to examine its effectiveness. The lithotypes considered included mafic (gabbronorite and hornblende gabbro) and ultramafic rocks (wehrlite, harzburgite, serpentinized dunite and chromitite). Based on the results, distributions of grayscale values are attributed to three main factors: (i) mineral phases with distinct attenuation coefficient and/or density properties i.e., plagioclase with mafic minerals or mafic minerals with high density oxides and/or spinel, (ii) coexistence of different mafic minerals or mafic with non-mafic phases, i.e., clinopyroxene present within gabbronorite or within peridotites, signifying the importance of predetermining the nature and composition of the rocks examined, (iii) mineral chemistry properties, i.e., variations of Ca and Al contents for plagioclase; Mg# variability mostly for orthopyroxene and olivine compared to clinopyroxene. Grain size variations between each mineral and their modal compositional modifications do not have a significant influence upon the distribution of grayscale values. Discrimination amongst the participating mineral phases in ophiolitic rocks is often challenging especially when the number of the participating minerals becomes significant, and even more when these display highly comparable attenuation coefficient and/or density properties. To overcome this barrier, this study suggests that a detailed petrographic examination along by deploying a series of systematic point counting microanalyses upon BSE images, can provide the necessary support to correctly define the grayscale properties of each individual mineral phase identified within the μCT images (see §3.2).

The ability of visualizing and analyzing with a non-destructive manner the internal mineral constituents of a rock sample is a main asset that X-ray micro-computed tomography (μCT) poses allowing to conduct advanced rock fabric analysis, which with other 2D techniques may are not able to be revealed. This was implemented to ophiolitic rocks of our study suite to identify deformation patterns and unravel mechanisms associated with emplacement through exhumation and overthrusting during the oceanic closure stage. Best-fit ellipsoids along with volume measurements contributed to the 3D morphology characterization of crystals and their orientation. Furthermore, fabric parameters (shape parameter T and anisotropy P′) were calculated based on the individual 3D-ellipsoids, allowing the evaluation of the fabric properties that grains of each mineral phase pose. Compared to conventional 2D methodologies applied upon thin sections, it is easier to conduct such analyses through μCT upon specified grain size distributions, to draw individual conclusions. Minor limitations may appear when grains form continuous network of aggregates or when microcracks are deployed, affecting to some degree the outcome correctness.

X-ray micro-computed tomography (μCT) coupled with mineral chemistry microanalyses is proposed as a tool for optimum characterization of ophiolitic rocks in a 3D perspective, which include accurate modal composition calculations, crystal structure and mineral distribution. Such information is critical to investigate ophiolitic rocks to resolve complex petrological and petrogenetic issues (mantle state, magma crystallization, deformation and/or alteration processes, identification of water-bearing phases, geodynamic implications) or for applied research purposes, including their usage as aggregates or to be considered as potential storage sites for CO_2 mineralization purposes to tackle climate change related problems.

Funding

This research did not receive any specific grant from funding agencies in the public, commercial, or not-for-profit sectors.

Declaration of Competing Interest

The authors declare that they have no known competing financial interests or personal relationships that could have appeared to influence the work reported in this paper.

Acknowledgments

We would like to acknowledge Mr. Gary Perrenoud (PIXE) for assisting in the μCT, as well as Dr. Vayia Xanthopoulou, Dr. Katerina Govatsi (LEMM) and Ms. Anna Mavridou (CERTH) for assisting in conducting mineral chemistry analyses. Many thanks are also given to Dr. Paraskevi Lampropoulou (UoP) and Mr. Apostolis Michopoulos (CERTH) for aiding in the XRD analyses. SGS Mineral Services, Canada is thanked for the QEMSCAN analyses. Prof. Dr. Sotiris Kokkalas (UoP) is likewise acknowledged for proving useful observations concerning the stereoplot results, as well as Prof. Dr. Dimitrios Papoulis and Asst. Prof. Dr. Stavros Kalaitzidis (UoP) for beneficial discussions and comments.

References

Aerden, D.G., Ruiz-Fuentes, A., 2020. X-ray computed micro-tomography of spiral garnets: a new test of how they form. J. Struct. Geol. 136.
Aerden, D.G.A.M., Ruiz-Fuentes, A., Sayab, M., Forde, A., 2021. Kinematics of subduction in the ibero-armorican arc constrained by 3D microstructural analysis of garnet and pseudomorphed lawsonite porphyroblasts from Île de Groix (Variscan belt). Solid Earth 12, 971–992.
Al-Khirbash, S.A., 2020. Mineralogical characterization of low-grade nickel laterites from the North Oman Mountains: using mineral liberation analyses – scanning electron microscopy-based automated quantitative mineralogy. Ore Geol. Rev. 120, 103429.
Baker, D.R., Mancini, L., Polacci, M., Higgins, M.D., Gualda, G.A.R., Hill, R.J., Rivers, M. L., 2012. An introduction to the application of X-ray microtomography to the three-dimensional study of igneous rocks. Lithos 148, 262–276.
Beccaluva, L., Coltorti, M., Saccani, E., Siena, F., 2005. Magma generation and crustal accretion as evidenced by supra-subduction ophiolites of the Albanide-Hellenide Subpelagonian zone. Island Arc 14, 551–563.
Beinlich, A., Plümper, O., Boter, E., Müller, I.A., Kourim, F., Ziegler, M., Harigane, Y., Lafay, R., Kelemen, P.B., 2020. Ultramafic rock carbonation: constraints from listvenite core BT1B, Oman Drilling Project. J. Geophys. Res. Solid Earth 125.

Bergqvist, M., Landström, E., Landström, E., Luth, S., 2019. Access to geological structures, density, minerals and textures through novel combination of 3D tomography, XRF and sample weight. ASEG Ext. Abstr. 2019, 1–3.
Bhanot, K.K., Downes, H., Petrone, C.M., Humphreys-Williams, E., 2017. Textures in spinel peridotite mantle xenoliths using micro-CT scanning: examples from Canary Islands and France. Lithos 276, 90–102.
Bhanot, K.K., Downes, H., Petrone, C.M., Humphreys-Williams, E., Clark, B., 2020. Micro-CT investigation of garnet-spinel clusters in mantle peridotite xenoliths. Lithos 352–353.
Bish, D.L., Post, J.E., 1993. Quantitative mineralogical analysis using the Rietveld full-pattern fitting method. Am. Mineral. 78, 932–940.
Bonev, N., Marchev, P., Moritz, R., Filipov, P., 2015. Timing of igneous accretion, composition, and temporal relation of the Kassandra–Sithonia rift-spreading center within the eastern Vardar suture zone, Northern Greece: insights into Jurassic arc/back-arc systems evolution at the Eurasian plate margin. Int. J. Earth Sci. 104, 1837–1864.
Boone, M., Dewanckele, J., Boone, M., Cnudde, V., Silversmit, G., Van Ranst, E., Jacobs, P., Vincze, L., Van Hoorebeke, L., 2011. Three-dimensional phase separation and identification in granite. Geosphere 7, 79–86.
Bortolotti, V., Chiari, M., Marroni, M., Pandolfi, L., Principi, G., Saccani, E., 2013. Geodynamic evolution of ophiolites from Albania and Greece (Dinaric-Hellenic belt): one, two, or more oceanic basins? Int. J. Earth Sci. 102, 783–811.
Callow, B., Falcon-Suarez, I., Ahmed, S., Matter, J., 2018. Assessing the carbon sequestration potential of basalt using X-ray micro-CT and rock mechanics. Int. J. Greenh. Gas Control 70, 146–156.
Carlson, W.D., 2006. Three-dimensional imaging of earth and planetary materials. Earth Planet. Sci. Lett. 249, 133–147.
Carlson, W.D., Rowe, T., Ketcham, R.A., Colbert, M.W., 2003. Applications of high-resolution X-ray computed tomography in petrology, meteoritics and palaeontology. Geol. Soc. Spec. Publ. 7–22.
Chatzaras, V., Kruckenberg, S.C., Cohen, S.M., Medaris, L.G., Withers, A.C., Bagley, B., 2016. Axial-type olivine crystallographic preferred orientations: the effect of strain geometry on mantle texture. J. Geophys. Res. Solid Earth 121, 4895–4922.
Christe, P., Turberg, P., Labiouse, V., Meuli, R., Parriaux, A., 2011. An X-ray computed tomography-based index to characterize the quality of cataclastic carbonate rock samples. Eng. Geol. 117, 180–188.
Christofides, G., Thimiatis, G., Koroneos, A., Sklavounos, S., Eleftheriadis, G., 1994. Mineralogy and chemistry of Cr-chlorites associated with chromites from Vavdos and Vasilika ophiolite complexes (Chalkidiki, Macedonia, N. Greece). Chem. Erde Geochem. 54, 151–166.
Cid, H.E., Carrasco-Núñez, G., Manea, V.C., 2017. Improved method for effective rock microporosity estimation using X-ray microtomography. Micron 97, 11–21.
Cnudde, V., Boone, M.N., 2013. High-resolution X-ray computed tomography in geosciences: a review of the current technology and applications. Earth Sci. Rev. 123, 1–17.
Corti, L., Zucali, M., Visalli, R., Mancini, L., Sayab, M., 2019. Integrating X-ray computed tomography with chemical imaging to quantify mineral re-crystallization from granulite to eclogite metamorphism in the Western Italian Alps (Sesia-Lanzo Zone). Front. Earth Sci. 7.
Danelian, T., Robertson, A.H.F., Dimitriadis, S., 1996. Age and significance of radiolarian sediments within basic extrusives of the marginal basin Guevgueli Ophiolite (northern Greece). Geol. Mag. 133, 127–136.
De Boever, W., Derluyn, H., Van Loo, D., Van Hoorebeke, L., Cnudde, V., 2015. Data-fusion of high resolution X-ray CT, SEM and EDS for 3D and pseudo-3D chemical and structural characterization of sandstone. Micron 74, 15–21.
Dijkstra, A.H., Drury, M.R., Vissers, R.L.M., Newman, J., 2002. On the role of melt-rock reaction in mantle shear zone formation in the Othris Peridotite Massif (Greece). J. Struct. Geol. 24, 1431–1450.
Dilek, Y., Furnes, H., 2011. Ophiolite genesis and global tectonics: geochemical and tectonic fingerprinting of ancient oceanic lithosphere. Bull. Geol. Soc. Am. 123, 387–411.
Dilek, Y., Furnes, H., Shallo, M., 2008. Geochemistry of the Jurassic Mirdita Ophiolite (Albania) and the MORB to SSZ evolution of a marginal basin oceanic crust. Lithos 100, 174–209.
Dilissen, N., Hidas, K., Garrido, C.J., López Sánchez-Vizcaíno, V., Kahl, W.A., 2021. Morphological transition during prograde olivine growth formed by high-pressure dehydration of antigorite-serpentinite to chlorite-harzburgite in a subduction setting. Lithos 382–383.
Đokić, O., Radević, A., Zakić, D., Đokić, B., 2020. Potential of natural and recycled concrete aggregate mixtures for use in pavement structures. Minerals 10, 1–16.
Emmanouilidis, A., Messaris, G., Ntzanis, E., Zampakis, P., Prevedouros, I., Bassukas, D. A., Avramidis, P., 2020. CT scanning, X-ray fluorescence: non-destructive techniques for the identification of sedimentary facies and structures. Rev. Micropaleontol. 67.
Fang, G., Ding, W., Liu, Y., Zhang, J., Xing, F., Dong, B., 2019. Identification of corrosion products and 3D distribution in reinforced concrete using X-ray micro computed tomography. Constr. Build. Mater. 207, 304–315.
FEI, 2019. Amira & Avizo 3D software.
Ferrière, J., Chanier, F., Ditbanjong, P., 2012. The Hellenic ophiolites: eastward or westward obduction of the Maliac Ocean, a discussion. Int. J. Earth Sci. 101, 1559–1580.
Fournari, R., Ioannou, I., Rigopoulos, I., 2021. The influence of ophiolitic crushed fine aggregate properties on the performance of cement mortars. Bull. Eng. Geol. Environ.
Friedrich, J.M., Wignarajah, D.P., Chaudhary, S., Rivers, M.L., Nehru, C.E., Ebel, D.S., 2008. Three-dimensional petrography of metal phases in equilibrated L chondrites-effects of shock loading and dynamic compaction. Earth Planet. Sci. Lett. 275, 172–180.
Gawrońska, A.C.L., Mcleod, Blumenfeld, E.H., Hanna, R.D., Zeigler, R.A., 2019. Preliminary Analyses of Apollo 15 Sample 15085 via X-Ray Computed Tomography, 50th Lunar and Planetary Science Conference 2019.
Giannakopoulou, P.P., Petrounias, P., Tsikouras, B., Kalaitzidis, S., Rogkala, A., Hatzipanagiotou, K., Tombros, S.F., 2018. Using factor analysis to determine the interrelationships between the engineering properties of aggregates from igneous rocks in Greece. Minerals 8.
Gillis, K., 1996. 3. Rare earth element constraints on the origin of amphibole in gabbroic rocks from site 894. Hess Deep 147.
Godel, B., 2013. High-resolution X-ray computed tomography and its application to ore deposits: from data acquisition to quantitative three-dimensional measurements with case studies from Ni-Cu-PGE Deposits. Econ. Geol. 108, 2005–2019.
Godel, B.M., Barnes, S.J., Barnes, S.J., 2013. Deposition mechanisms of magmatic sulphide liquids: evidence from high-resolution x-ray computedtomography andtrace element chemistry of komatiite-hosted disseminated sulphides. J. Petrol. 54, 1454–1481.
Godinho, J.R.A., Kern, M., Renno, A.D., Gutzmer, J., 2019. Volume quantification in interphase voxels of ore minerals using 3D imaging. Miner. Eng. 144.
Gomila, R., Arancibia, G., Mery, D., Nehler, M., Bracke, R., Morata, D., 2019. Palaeopermeability anisotropy and geometrical properties of sealed-microfractures from micro-CT analyses: an open-source implementation. Micron 117, 29–39.
Gomila, R., Arancibia, G., Nehler, M., Bracke, R., Morata, D., Cembrano, J., 2021. Quantitative anisotropies of palaeopermeability in a strike-slip fault damage zone: insights from micro-CT analysis and numerical simulations. Tectonophysics 810, 228873.
Gottlieb, P., Wilkie, G., Sutherland, D., Ho-Tun, E., Suthers, S., Perera, K., Jenkins, B., Spencer, S., Butcher, A., Rayner, J., 2000. Using quantitative electron microscopy for process mineralogy applications. JOM 52, 24–25.
Grammatikopoulos, T.A., Kapsiotis, A., Tsikouras, B., Hatzipanagiotou, K., Zaccarini, F., Garuti, G., 2011. Spinel composition, PGE geochemistry and mineralogy of the chromitites from the vourinos ophiolite complex, northwestern Greece. Canad. Mineral. 49, 1571–1598.
Guntoro, P.I., Ghorbani, Y., Koch, P.H., Rosenkranz, J., 2019. X-ray microcomputed tomography (μct) for mineral characterization: a review of data analysis methods. Minerals 9.
Hanna, R.D., Ketcham, R.A., 2017. X-ray computed tomography of planetary materials: a primer and review of recent studies. Chem. Erde 77, 547–572.
Herrmann, W., Berry, R.F., 2002. MINSQ - a least squares spreadsheet method for calculating mineral proportions from whole rock major element analyses. Geochem. Explor. Environ. Anal. 2, 361–368.
Hoal, K.O., Stammer, J.G., Appleby, S.K., Botha, J., Ross, J.K., Botha, P.W., 2009. Research in quantitative mineralogy: examples from diverse applications. Miner. Eng. 22, 402–408.
Horton, F., Farley, K., Jackson, M., 2019. Helium distributions in ocean island basalt olivines revealed by X-ray computed tomography and single-grain crushing experiments. Geochim. Cosmochim. Acta 244, 467–477.
Howarth, G.H., Sobolev, N.V., Pernet-Fisher, J.F., Ketcham, R.A., Maisano, J.A., Pokhilenko, L.N., Taylor, D., Taylor, L.A., 2015. 3-D X-ray tomography of diamondiferous mantle eclogite xenoliths, Siberia: a review. J. Asian Earth Sci. 101, 39–67.
Howarth, G.H., Udry, A., Day, J.M.D., 2018. Petrogenesis of basaltic shergottite Northwest Africa 8657: implications for fO2 correlations and element redistribution during shock melting in shergottites. Meteor. Planet. Sci. 53, 249–267.
Huisman, D.J., Ngan-Tillard, D., Tensen, M.A., Laarman, F.J., Raemaekers, D.C.M., 2014. A question of scales: studying Neolithic subsistence using micro CT scanning of midden deposits. J. Archaeol. Sci. 49, 585–594.
Ishimaru, S., Arai, S., Tamura, A., 2017. Clinopyroxenite dykes within a banded unit in the basal mantle section of the northern part of the Oman ophiolite: a record of the latest deep-seated magmatism. Lithos 292–293, 334–347.
Jardine, M.A., Miller, J.A., Becker, M., 2018. Coupled X-ray computed tomography and grey level co-occurrence matrices as a method for quantification of mineralogy and texture in 3D. Comput. Geosci. 111, 105–117.
Jerram, D.A., Davis, G.R., Mock, A., Charrier, A., Marsh, B.D., 2010. Quantifying 3D crystal populations, packing and layering in shallow intrusions: a case study from the Basement Sill, Dry Valleys, Antarctica. Geosphere 6, 537–548.
Kahl, W.A., Dilissen, N., Hidas, K., Garrido, C.J., LÓpez-SÁnchez-Vizcaíno, V., RomÁn-Alpiste, M., 2017. 3-D microstructure of olivine in complex geological materials reconstructed by correlative X-ray μ-CT and EBSD analyses. J. Microsc. 268, 193–207.
Kelektsoglou, K., 2018. Carbon capture and storage: a review of mineral storage of CO_2 in Greece. Sustainability 10.
Ketcham, R.A., 2005a. Computational methods for quantitative analysis of three-dimensional features in geological specimens. Geosphere 1, 32–41.
Ketcham, R.A., 2005b. Three-dimensional grain fabric measurements using high-resolution X-ray computed tomography. J. Struct. Geol. 27, 1217–1228.
Ketcham, R.A., Carlson, W.D., 2001. Acquisition, optimization and interpretation of x-ray computed tomographic imagery: applications to the geosciences. Comput. Geosci. 27, 381–400.
Koukouzas, N., Koutsovitis, P., Tyrologou, P., Karkalis, C., Arvanitis, A., 2019. Potential for mineral carbonation of co2 in pleistocene basaltic rocks in volos region (Central greece). Minerals 9.
Koutsovitis, P., 2012. Gabbroic rocks in ophiolitic occurrences from East Othris, Greece: petrogenetic processes and geotectonic environment implications. Mineral. Petrol. 104, 249–265.

Koutsovitis, P., Magganas, A., 2016. Boninitic and tholeiitic basaltic lavas and dikes from dispersed Jurassic East Othris ophiolitic units, Greece: petrogenesis and geodynamic implications. Int. Geol. Rev. 58, 1983–2006.
Kuper, K.E., Zedgenizov, D.A., Ragozin, A.L., Shatsky, V.S., Porosev, V.V., Zolotarev, K. V., Babichev, E.A., Ivanov, S.A., 2007. Three-dimensional distribution of minerals in diamondiferous eclogites, obtained by the method of high-resolution X-ray computed tomography. Nucl. Instrum. Methods Phys. Res. Sect. A Accel. Spectrom. Detectors Assoc. Equip. 575, 255–258.
Kyle, J.R., Ketcham, R.A., 2015. Application of high resolution X-ray computed tomography to mineral deposit origin, evaluation, and processing. Ore Geol. Rev. 65, 821–839.
Lafay, R., Fernandez-Martinez, A., Montes-Hernandez, G., Auzende, A.L., Poulain, A., 2016. Dissolution-reprecipitation and self-assembly of serpentine nanoparticles preceding chrysotile formation: insights into the structure of proto-serpentine. Am. Mineral. 101, 2666–2676.
Lai, J., Wang, G., Fan, Z., Chen, J., Qin, Z., Xiao, C., Wang, S., Fan, X., 2017. Three-dimensional quantitative fracture analysis of tight gas sandstones using industrial computed tomography. Sci. Rep. 7.
Lampropoulou, P., Petrounias, P., Giannakopoulou, P.P., Rogkala, A., Koukouzas, N., Tsikouras, B., Hatzipanagiotou, K., 2020. The effect of chemical composition of ultramafic and mafic aggregates on their physicomechanical properties as well as on the produced concrete strength. Minerals 10.
Langheinrich, A.C., Wienhard, J., Vormann, S., Hau, B., Bohle, R.M., Zygmunt, M., 2004. Analysis of the fetal placental vascular tree by X-ray micro-computed tomography. Placenta 25, 95–100.
Larrea, M.L., Castro, S.M., Bjerg, E.A., 2014. A software solution for point counting. Petrographic thin section analysis as a case study. Arab. J. Geosci. 7, 2981–2989.
Lätti, D., Adair, B.J.I., 2001. An assessment of stereological adjustment procedures. Miner. Eng. 14, 1579–1587.
Le Bayon, R.C., Guenat, C., Schlaepfer, R., Fischer, F., Luiset, A., Schomburg, A., Turberg, P., 2021. Use of X-ray microcomputed tomography for characterizing earthworm-derived belowground soil aggregates. Eur. J. Soil Sci. 72, 1113–1127.
Liernur, A., Schomburg, A., Turberg, P., Guenat, C., Le Bayon, R.C., Brunner, P., 2017. Coupling X-ray computed tomography and freeze-coring for the analysis of fine-grained low-cohesive soils. Geoderma 308, 171–186.
Liu, Y., Dai, F., 2021. A review of experimental and theoretical research on the deformation and failure behavior of rocks subjected to cyclic loading. J. Rock Mech. Geotech. Eng. 13, 1203–1230.
Lu, H.-Y., Lin, C.-K., Lin, W., Liou, T.-S., Chen, W.-F., Chang, P.-Y., 2011. A natural analogue for CO_2 mineral sequestration in Miocene basalt in the Kuanhsi-Chutung area, Northwestern Taiwan. Int. J. Greenh. Gas Control 5, 1329–1338.
Magganas, A., Koutsovitis, P., 2015. Composition, melting and evolution of the upper mantle beneath the Jurassic Pindos ocean inferred by ophiolitic ultramafic rocks in East Othris, Greece. Int. J. Earth Sci. 104, 1185–1207.
Maurício, A., Pereira, M.F., Rocha, C., Figueiredo, C., Marques, J.M., 2017. X-ray micro-CT study of Cabeço de Vide Serpentinites and carbonate rock samples: a preliminary approach. Procedia Earth Planet. Sci. 17, 952–955.
Mayhew, L.E., Ellison, E.T., Miller, H.M., Kelemen, P.B., Templeton, A.S., 2018. Iron transformations during low temperature alteration of variably serpentinized rocks from the Samail ophiolite, Oman. Geochim. Cosmochim. Acta 222, 704–728.
Mehdikhani, M., Straumit, I., Gorbatikh, L., Lomov, S.V., 2019. Detailed characterization of voids in multidirectional carbon fiber/epoxy composite laminates using X-ray micro-computed tomography. Compos. Part A Appl. Sci. Manuf. 125.
Michard, A., Feinberg, H., Montigny, R., 1998. Supra-ophiolitic formations from the Thessaloniki nappe (Greece), and associated magmatism: an intra-oceanic subduction predates the Vardar obduction. Comptes Rendus de l'Academie de. Sciences Serie IIa Sciences de la Terre et des Planetes 327, 493–499.
Milatz, M., Hüsener, N., Andò, E., Viggiani, G., Grabe, J., 2021. Quantitative 3D imaging of partially saturated granular materials under uniaxial compression. Acta Geotech. 16, 3573–3600.
Militello, G.M., Bloise, A., Gaggero, L., Lanzafame, G., Punturo, R., 2019. Multi-analytical approach for asbestos minerals and their non-asbestiform analogues: inferences from host rock textural constraints. Fibers 7.
Miller, H.M., Mayhew, L.E., Ellison, E.T., Kelemen, P., Kubo, M., Templeton, A.S., 2017. Low temperature hydrogen production during experimental hydration of partially-serpentinized dunite. Geochim. Cosmochim. Acta 209, 161–183.
Miller, J.D., Lin, C.L., 2004. Three-dimensional analysis of particulates in mineral processing systems by cone beam X-ray microtomography. Miner. Metall. Process. 21, 113–124.
Miller, K.J., Zhu, W.L., Montési, L.G.J., Gaetani, G.A., Le Roux, V., Xiao, X., 2016. Experimental evidence for melt partitioning between olivine and orthopyroxene in partially molten harzburgite. J. Geophys. Res. Solid Earth 121, 5776–5793.
Mock, K., Amato, J., Bertmaring, J., 2012. GeoPixelCounter 1.0 ed.
Morimoto, N., 1988. Nomenclature of pyroxenes. Mineral. Petrol. 39, 55–76.
Mote, A.S., Ketcham, R.A., Watson, W.P., 2010. Extracting particle orientations from three-dimensional datasets using BLOB3D. Adv. X-ray Tomogr. Geomater. 407–413.
Munawar, M.J., Lin, C., Cnudde, V., Bultreys, T., Dong, C., Zhang, X., De Boever, W., Zahid, M.A., Wu, Y., 2018. Petrographic characterization to build an accurate rock model using micro-CT: case study on low-permeable to tight turbidite sandstone from Eocene Shahejie Formation. Micron 109, 22–33.
Ngan-Tillard, D.J.M., Huisman, D.J., Corbella, F., Van Nass, A., 2018. Over the rainbow? Micro-CT scanning to non-destructively study Roman and early medieval glass bead manufacture. J. Archaeol. Sci. 98, 7–21.
Noël, J., Godard, M., Oliot, E., Martinez, I., Williams, M., Boudier, F., Rodriguez, O., Chaduteau, C., Escario, S., Gouze, P., 2018. Evidence of polygenetic carbon trapping in the Oman Ophiolite: petro-structural, geochemical, and carbon and oxygen isotope study of the Wadi Dima harzburgite-hosted carbonates (Wadi Tayin massif, Sultanate of Oman). Lithos 323, 218–237.
Noiriel, C., 2015. Resolving time-dependent evolution of pore-scale structure, permeability and reactivity using X-ray microtomography. Rev. Mineral. Geochem. 247–285.
Okazaki, K., Michibayashi, K., Hatakeyama, K., Abe, N., Johnson, K.T.M., Kelemen, P.B., Team, t.O.D.P.S, 2021. Major mineral fraction and physical properties of carbonated peridotite (Listvenite) from ICDP Oman Drilling Project Hole BT1B inferred from X-Ray CT core images. J. Geophys. Res. Solid Earth 126, e2021JB022719.
Pankhurst, M.J., Dobson, K.J., Morgan, D.J., Loughlin, S.C., Thordarson, T., Lee, P.D., Courtois, L., 2014. Monitoring the magmas fuelling volcanic eruptions in near-real-time using X-ray micro-computed tomography. J. Petrol. 55, 671–684.
Pankhurst, M.J., Vo, N.T., Butcher, A.R., Long, H., Wang, H., Nonni, S., Harvey, J., Gucrossed, G.D.S., Fowler, R., Atwood, R., Walshaw, R., Lee, P.D., 2018. Quantitative measurement of olivine composition in three dimensions using helical-scan X-ray micro-tomography. Am. Mineral. 103, 1800–1811.
Parisatto, M., Turina, A., Cruciani, G., Mancini, L., Peruzzo, L., Cesare, B., 2018. Three-dimensional distribution of primary melt inclusions in garnets by X-ray microtomography. Am. Mineral. 103, 911–926.
Pascoe, R.D., Power, M.R., Simpson, B., 2007. QEMSCAN analysis as a tool for improved understanding of gravity separator performance. Miner. Eng. 20, 487–495.
Patkó, L., Créon, L., Kovács, Z., Liptai, N., Rosenberg, E., Szabó, C., 2020. Three-dimensional distribution of glass and vesicles in metasomatized xenoliths: a micro-CT case study from Nógrád-Gömör volcanic field (Northern Pannonian Basin). Geol. Carpath. 71, 418–423.
Petri, B., Almqvist, B.S.G., Pistone, M., 2020. 3D rock fabric analysis using micro-tomography: an introduction to the open-source TomoFab MATLAB code. Comput. Geosci. 138.
Petrounias, P., Giannakopoulou, P.P., Rogkala, A., Stamatis, P.M., Lampropoulou, P., Tsikouras, B., Hatzipanagiotou, K., 2018. The effect of petrographic characteristics and physico-mechanical properties of aggregates on the quality of concrete. Minerals 8.
Peuble, S., Andreani, M., Gouze, P., Pollet-Villard, M., Reynard, B., Van de Moortele, B., 2018. Multi-scale characterization of the incipient carbonation of peridotite. Chem. Geol. 476, 150–160.
Pomonis, P., Rigopoulos, I., Tsikouras, B., Hatzipanagiotou, K., 2007. Relationships between petrographic and physicomechanical properties of basic igneous rocks from the pindos ophiolitic complex, NW Greece 2007 (40), 12.
Popov, O., Talovina, I., Lieberwirth, H., Duriagina, A., 2020. Quantitative microstructural analysis and X-ray computed tomography of ores and rocks—comparison of results. Minerals 10, 129.
Porfido, C., Manzari, P., Allegretta, I., Terzano, R., De Pascale, O., Senesi, G.S., 2020. Combined micro X-ray fluorescence and micro computed tomography for the study of extraterrestrial volcanic rocks. The case of North West Africa (NWA) 8657: a shergottite martian meteorite. Talanta 217.
Prichard, H.M., Barnes, S.J., Godel, B., Reddy, S.M., Vukmanovic, Z., Halfpenny, A., Neary, C.R., Fisher, P.C., 2015. The structure of and origin of nodular chromite from the Troodos ophiolite, Cyprus, revealed using high-resolution X-ray computed tomography and electron backscatter diffraction. Lithos 218–219, 87–98.
Prichard, H.M., Barnes, S.J., Dale, C.W., Godel, B., Fisher, P.C., Nowell, G.M., 2017. Paragenesis of multiple platinum-group mineral populations in Shetland ophiolite chromitite: 3D X-ray tomography and in situ Os isotopes. Geochim. Cosmochim. Acta 216, 314–334.
Prichard, H.M., Barnes, S.J., Godel, B., 2018. A mechanism for chromite growth in ophiolite complexes: evidence from 3D high-resolution X-ray computed tomography images of chromite grains in Harold's Grave chromitite in the Shetland ophiolite. Mineral. Mag. 82, 457–470.
Prodanović, M., Mehmani, A., Sheppard, A.P., 2015. Imaged-based Multiscale Network Modelling of Microporosity in Carbonates, 406. Geological Society, Special Publications, London, p. 95.
Rassios, A., Tzamos, E., Dilek, Y., Bussolesi, M., Grieco, G., Batsi, A., Gamaletsos, P.N., 2020. A structural approach to the genesis of chrome ores within the Vourinos ophiolite (Greece): significance of ductile and brittle deformation processes in the formation of economic ore bodies in oceanic upper mantle peridotites. Ore Geol. Rev. 125.
Rassios, A.H.E., Moores, E.M., 2006. Heterogeneous Mantle Complex, Crustal Processes, and Obduction Kinematics in a Unified Pindos - Vourinos ophiolitic slab (Northern Greece). Geological Society Special Publication, pp. 237–266.
Reyes, F., Lin, Q., Udoudo, O., Dodds, C., Lee, P.D., Neethling, S.J., 2017. Calibrated X-ray micro-tomography for mineral ore quantification. Min. Eng. 110, 122–130.
Richard, A., Morlot, C., Créon, L., Beaudoin, N., Balistky, V.S., Pentelei, S., Dyja-Person, V., Giuliani, G., Pignatelli, I., Legros, H., Sterpenich, J., Pironon, J., 2019. Advances in 3D imaging and volumetric reconstruction of fluid and melt inclusions by high resolution X-ray computed tomography. Chem. Geol. 508, 3–14.
Roduit, N., 2019. JMicroVision: Image analysis toolbox for measuring and quantifying components of high-definition images., 1.3.4 ed.
Rogkala, A., Petrounias, P., Tsikouras, B., Giannakopoulou, P.P., Hatzipanagiotou, K., 2019. Mineralogical evidence for partial melting and melt-rock interaction processes in the mantle peridotites of edessa ophiolite (North Greece). Minerals 9.
Sahiström, F., Jonsson, E., Högdahl, K., Ghaderidosst, J., Luth, S., Lynch, E., Landström, E., Sädbom, S., 2019. Textural evolution of the Lovisa Zn-Pb-(Ag) deposit, Bergslagen, Sweden: insights from microscopy and 3D X-ray tomography. In: 15th SGA Biennial Meeting on Life with Ore Deposits on Earth, AUG 27–30, 2019, Univ Glasgow, Glasgow, Scotland. Soc Geology Applied Mineral Deposits-SGA, pp. 443–446.

Sarno, A., Mettivier, G., Di Lillo, F., Cesarelli, M., Bifulco, P., Russo, P., 2016. Cone-beam micro computed tomography dedicated to the breast. Med. Eng. Phys. 38, 1449–1457.
Sayab, M., Miettinen, A., Aerden, D., Karell, F., 2017. Orthogonal switching of AMS axes during type-2 fold interference: insights from integrated X-ray computed tomography, AMS and 3D petrography. J. Struct. Geol. 103, 1–16.
Sayab, M., Aerden, D., Kuva, J., Hassan, W.U., 2021. Tectonic evolution of the Karakoram metamorphic complex (NW Himalayas) reflected in the 3D structures of spiral garnets: Insights from X-ray computed micro-tomography. Geosci. Front. 12.
Schindelin, J., Arganda-Carreras, I., Frise, E., Kaynig, V., Longair, M., Pietzsch, T., Preibisch, S., Rueden, C., Saalfeld, S., Schmid, B., Tinevez, J.Y., White, D.J., Hartenstein, V., Eliceiri, K., Tomancak, P., Cardona, A., 2012. Fiji: an open-source platform for biological-image analysis. Nat. Method 9, 676–682.
Schladitz, K., 2011. Quantitative micro-CT. J. Microsc. 243, 111–117.
Šegvić, B., Lugović, B., Slovenec, D., Meyer, H.P., 2016. Mineralogy, petrology and geochemistry of amphibolites from the Kalnik Mt. (Sava Unit, North Croatia): implications for the evolution of north-westernmost part of the Dinaric-Vardar branch of Mesozoic Tethys. Ofioliti 41, 35–58.
Sideridis, A., Zaccarini, F., Grammatikopoulos, T., Tsitsanis, P., Tsikouras, B., Pushkarev, E., Garuti, G., Hatzipanagiotou, K., 2018. First occurrences of ni-phosphides in chromitites from the ophiolite complexes of alapaevsk, Russia and gerakini-ormylia, Greece. Ofioliti 43, 75–84.
Sideridis, A., Zaccarini, F., Koutsovitis, P., Grammatikopoulos, T., Tsikouras, B., Garuti, G., Hatzipanagiotou, K., 2021. Chromitites from the Vavdos ophiolite (Chalkidiki, Greece): petrogenesis and geotectonic settings; constrains from spinel, olivine composition, PGE mineralogy and geochemistry. Ore Geol. Rev. 137.
Snæbjörnsdóttir, S.Ó., Sigfússon, B., Marieni, C., Goldberg, D., Gislason, S.R., Oelkers, E. H., 2020. Carbon dioxide storage through mineral carbonation. Nat. Rev. Earth Environ. 1, 90–102.
Sutherland, D., 2007. Estimation of mineral grain size using automated mineralogy. Miner. Eng. 20, 452–460.
Suuronen, J.P., Sayab, M., 2018. 3D nanopetrography and chemical imaging of datable zircons by synchrotron multimodal X-ray tomography. Sci. Rep. 8, 4747.
Tilhac, R., Ceuleneer, G., Griffin, W.L., O'Reilly, S.Y., Pearson, N.J., Benoit, M., Henry, H., Girardeau, J., Grégoire, M., 2016. Primitive arc magmatism and delamination: petrology and geochemistry of pyroxenites from the Cabo Ortegal Complex, Spain. J. Petrol. 57, 1921–1954.
Tominaga, M., Ortiz, E., Einsle, J.F., Ryoichi Vento, N.F., Schrenk, M.O., Buisman, I., Ezad, I.S., Cardace, D., 2021. Tracking subsurface active weathering processes in serpentinite. Geophys. Res. Lett. 48.
Tribuzio, R., Tiepolo, M., Thirlwall, M.F., 2000. Origin of titanian pargasite in gabbroic rocks from the Northern Apennine ophiolites (Italy): insights into the late-magmatic evolution of a MOR-type intrusive sequence. Earth Planet. Sci. Lett. 176, 281–293.
Tripathy, S.K., Murthy, Y.R., Singh, V., Farrokhpay, S., Filippov, L.O., 2019. Improving the quality of ferruginous chromite concentrates via physical separation methods. Minerals 9, 667.
Tsuchiyama, A., Hanamoto, T., Nakashima, Y., Nakano, T., 2000. Quantitative evaluation of attenuation contrast of minerals by using a medical X-ray CT scanner. J. Mineral. Petrol. Sci. 95, 125–137.
Tsuchiyama, A., Nakamura, T., Nakano, T., Nakamura, N., 2002. Three-dimensional description of the Kobe meteorite by micro X-ray CT method: possibility of three-dimensional curation of meteorite samples. Geochem. J. 36, 369–390.
Tuniz, C., Zanini, F., 2018. Microcomputerized Tomography (MicroCT) in Archaeology, Encyclopedia of Global Archaeology. Springer International Publishing, Cham, pp. 1–7.
Turberg, P., Zeimetz, F., Grondin, Y., Elandoy, C., Buttler, A., 2014. Characterization of structural disturbances in peats by X-ray CT-based density determinations. Eur. J. Soil Sci. 65, 613–624.
Uemura, S., Kataoka, R., Fukabori, D., Tsushima, S., Hirai, S., 2011. Experiment on liquid and supercritical CO_2 distribution using micro-focus X-ray CT for estimation of geological storage. Energy Procedia 5102–5107.
Uesugi, M., Uesugi, K., Oka, M., 2010. Non-destructive observation of meteorite chips using quantitative analysis of optimized X-ray micro-computed tomography. Earth Planet. Sci. Lett. 299, 359–367.
Voltolini, M., Kwon, T.H., Ajo-Franklin, J., 2017. Visualization and prediction of supercritical CO_2 distribution in sandstones during drainage: an in situ synchrotron X-ray micro-computed tomography study. Int. J. Greenh. Gas Control 66, 230–245.
Wang, Y., Miller, J.D., 2020. Current developments and applications of micro-CT for the 3D analysis of multiphase mineral systems in geometallurgy. Earth Sci. Rev. 211.
Warlo, M., Wanhainen, C., Bark, G., Butcher, A.R., McElroy, I., Brising, D., Rollinson, G. K., 2019. Automated quantitative mineralogy optimized for simultaneous detection of (precious/critical) rare metals and base metals in a production-focused environment. Minerals 9, 440.
Warlo, M., Bark, G., Wanhainen, C., Butcher, A.R., Forsberg, F., Lycksam, H., Kuva, J., 2021. Multi-scale X-ray computed tomography analysis to aid automated mineralogy in ore geology research. Front. Earth Sci. 9.
Whattam, S.A., Stern, R.J., 2011. The 'subduction initiation rule': a key for linking ophiolites, intra-oceanic forearcs, and subduction initiation. Contrib. Mineral. Petrol. 162, 1031–1045.
Whitney, D.L., Evans, B.W., 2010. Abbreviations for names of rock-forming minerals. Am. Mineral. 95, 185–187.
Wildenschild, D., Sheppard, A.P., 2013. X-ray imaging and analysis techniques for quantifying pore-scale structure and processes in subsurface porous medium systems. Adv. Water Resour. 51, 217–246.
Yan, S., Adegbule, A., Kibbey, T.C.G., 2017. A hybrid 3D SEM reconstruction method optimized for complex geologic material surfaces. Micron 99, 26–31.
Yang, P., Elhajjar, R., 2014. Porosity content evaluation in carbon-fiber/epoxy composites using X-ray computed tomography. Polym. Plastics Technol. Eng. 53, 217–222.
Yang, S.-Q., Tian, W.-L., Ranjith, P.G., 2017. Experimental investigation on deformation failure characteristics of crystalline marble under triaxial cyclic loading. Rock Mech. Rock Eng. 50, 2871–2889.
Yu, Y., Xu, W.L., Wang, C.G., 2014. Experimental studies of melt-peridotite reactions at 1–2 GPa and 1250–1400 °C and their implications for transforming the nature of lithospheric mantle and for high-Mg signatures in adakitic rocks. Sci. China Earth Sci. 57, 415–427.
Zachariadis, P., Kostopoulos, D., Reischmann, T., Himmerkus, F., Matukov, D., Sergeev, S., 2006. U-Pb ion-microprobe zircon dating of subduction-related magmatism from northern Greece: the ages of the Guevgueli, Thessaloniki and Chalkidiki igneous complexes. Geophys. Res. Abstr. 05560.
Zhang, P., Lee, Y.I., Zhang, J., 2019. A review of high-resolution X-ray computed tomography applied to petroleum geology and a case study. Micron 124.
Zoheir, B., Diab, A., Koutsovitis, P., Alam, T.A., Feigenson, M., El-Bialy, M., Abdelnasser, A., 2022. Mantle source heterogeneity in a Neoproterozoic back-arc basin: geochemical and thermodynamic modeling of the volcanic section of Wadi Ghadir ophiolite, Egypt. Precambrian Res. 368, 106480.
Zucali, M., Voltolini, M., Ouladdiaf, B., Mancini, L., Chateigner, D., 2014. The 3D quantitative lattice and shape preferred orientation of a mylonitised metagranite from Monte Rosa (Western Alps): combining neutron diffraction texture analysis and synchrotron X-ray microtomography. J. Struct. Geol. 63, 91–105.